2021

Dynamically linking influenza virus infection kinetics, lung injury, inflammation, and disease severity

Margaret A. Myers

Amanda P. Smith

Lindey C. Lane

David J. Moquin

Rosemary Aogo

See next page for additional authors

Authors

Margaret A. Myers, Amanda P. Smith, Lindey C. Lane, David J. Moquin, Rosemary Aogo, Stacie Woolard, Paul Thomas, Peter Vogel, and Amber M. Smith

Dynamically linking influenza virus infection kinetics, lung injury, inflammation, and disease severity

Margaret A Myers[1†], Amanda P Smith[1†], Lindey C Lane[1], David J Moquin[2], Rosemary Aogo[1], Stacie Woolard[3], Paul Thomas[4], Peter Vogel[5], Amber M Smith[1]*

[1]Department of Pediatrics, University of Tennessee Health Science Center, Memphis, United States; [2]Department of Anesthesiology, Washington University School of Medicine, St. Louis, United States; [3]Flow Cytometry Core, St. Jude Children's Research Hospital, Memphis, United States; [4]Department of Immunology, St. Jude Children's Research Hospital, Memphis, United States; [5]Department of Pathology, St. Jude Children's Research Hospital, Memphis, United States

Abstract Influenza viruses cause a significant amount of morbidity and mortality. Understanding host immune control efficacy and how different factors influence lung injury and disease severity are critical. We established and validated dynamical connections between viral loads, infected cells, CD8^{+} T cells, lung injury, inflammation, and disease severity using an integrative mathematical model-experiment exchange. Our results showed that the dynamics of inflammation and virus-inflicted lung injury are distinct and nonlinearly related to disease severity, and that these two pathologic measurements can be independently predicted using the model-derived infected cell dynamics. Our findings further indicated that the relative CD8^{+} T cell dynamics paralleled the percent of the lung that had resolved with the rate of CD8^{+} T cell-mediated clearance rapidly accelerating by over 48,000 times in 2 days. This complimented our analyses showing a negative correlation between the efficacy of innate and adaptive immune-mediated infected cell clearance, and that infection duration was driven by CD8^{+} T cell magnitude rather than efficacy and could be significantly prolonged if the ratio of CD8^{+} T cells to infected cells was sufficiently low. These links between important pathogen kinetics and host pathology enhance our ability to forecast disease progression, potential complications, and therapeutic efficacy.

Introduction

Over 15 million respiratory infections and 200,000 hospitalizations result from influenza A viruses (IAVs) each year (*Thompson et al., 2004*; *Simonsen et al., 2000*; *Taubenberger and Morens, 2008*; *Medina and García-Sastre, 2011*). The incidence and severity of IAV infections increases when new strains emerge and/or when there is a lack of prior immunity. A robust immune response is crucial for resolving viral infections, but immune-mediated pathology can exacerbate disease (*Duan and Thomas, 2016*; *Moskophidis and Kioussis, 1998*; *Mauad et al., 2010*; *Rygiel et al., 2009*; *La Gruta et al., 2007*). High viral loads can also play a role in disease progression (*Boon et al., 2011*; *de Jong et al., 2006*), but these do not always correlate with the strength of the host response or with disease severity (*Granados et al., 2017*; *Marathe et al., 2016*; *Toapanta and Ross, 2009*; *Smith et al., 2019*; *Gao et al., 2013*). An understanding of how viral loads, host immune responses, and disease progression are related is critical to identify disease-specific markers that may help predict hospitalization or other complications.

During IAV infection in both humans and animals, viral loads increase rapidly for the first 1–2 days of infection before reaching a peak (e.g., as in *Smith et al., 2018*; *Baccam et al., 2006*; *Miao et al., 2010*; *Toapanta and Ross, 2009*; *Carrat et al., 2008*; *Srivastava et al., 2009*; *Gao et al., 2013*). If the host is infected with a novel strain or has no prior immunity, viral loads in the lung then begin to decline, first slowly (sometimes <1 $\log_{10}$ TCID$_{50}$/d) then rapidly (> 4-5 $\log_{10}$ TCID$_{50}$/d) (*Smith et al., 2018*; *Gao et al., 2013*). We previously quantified this biphasic viral decline with a mathematical model, which indicated that the rate of infected cell clearance increases as the density of infected cells decreases (*Smith et al., 2018*). The timing of the second, rapid viral decay phase coincides with the expansion of CD8$^+$ T cells, which are the primary cell responsible for clearing infected cells and resolving the infection (*Zhang and Bevan, 2011*; *Chen et al., 2018*; *McMichael et al., 1983*; *La Gruta and Turner, 2014*; *Kreijtz et al., 2011*), and, to a lesser extent, neutralizing antibodies (*Chen et al., 2018*; *Kreijtz et al., 2011*; *Fang and Sigal, 2005*; *Wang et al., 2015*; *McMichael et al., 1983*) and cytotoxic CD4$^+$ T cells (*Wilkinson et al., 2012*). For the CD8$^+$ T cell response, in particular, it remains unclear whether the efficacy of these cells is dictated by their own density (*Graw and Regoes, 2009*; *Wiedemann et al., 2006*), infected cell density (*Merrill, 1982*; *Caramalho et al., 2009*; *Halle et al., 2016*), or both (*Gadhamsetty et al., 2014*). While quantifying dynamically changing CD8$^+$ T cell efficacy is difficult *in vitro* and *in vivo*, the question is ripe for *in silico* investigation. Several modeling studies have described CD8$^+$ T cell-mediated infected cell clearance for various viral infections in humans and animals, including IAV, HIV, and LCMV (e.g., as in *Ganusov et al., 2011*; *De Boer and Perelson, 1998*; *Perelson and Bell, 1982*; *Miao et al., 2010*; *Cao et al., 2016*; *Lee et al., 2009*; *Price et al., 2015*; *Graw and Regoes, 2009*; *Merrill, 1982*; *Gadhamsetty et al., 2014*; *Baral et al., 2019*; *Bonhoeffer et al., 2000*; *Conway and Perelson, 2015*). Some of these studies have also attempted to link this response and other immune responses to inflammation or disease severity (*Price et al., 2015*; *Baral et al., 2019*; *Manchanda et al., 2014*), but have not yet found the appropriate mathematical relation with the available data. In addition, for IAV infections in particular, varied efficiency of the CD8$^+$ T cell response throughout the course of infection, their early antigen-specific and lung-resident responses (*Yoon et al., 2007*; *McGill and Legge, 2009*; *Keating et al., 2018*), and the balanced consequences on viral loads and host pathology have not yet been investigated in detail.

A better understanding of infected cell clearance may also yield insight into the damage induced to the lung and the ensuing immunopathology during IAV infection. In general, widespread alveolar disease is observed in patients who succumb to the infection (*Bautista et al., 2010*; *Shieh et al., 2010*; *Gao et al., 2013*), and CT scans show bilateral and multi-focal areas of lung damage (e.g. as in *Kohr et al., 2010*; *Li et al., 2011*; *Ajlan et al., 2009*; *Soto-Abraham et al., 2009*; *Gill et al., 2010*; *Li et al., 2012*). Further, hospitalized patients that died as a result from infection with the 2009 H1N1 influenza virus had large numbers of CD8$^+$ T cells present in their lung tissue (*Mauad et al., 2010*). Large pulmonary populations of CD8$^+$ T cells contribute to lung injury by targeting IAV-infected cells (reviewed in *Duan and Thomas, 2016*) and inducing 'bystander damage' to uninfected epithelial cells (*van de Sandt et al., 2017*). However, their population levels do not necessarily indicate active infected cell removal or immunopathology as their extended presence in the lung also contributes to surveillance and repair (*Matheu et al., 2013*; *Sun et al., 2009*). Macrophages and neutrophils also persist in the lung following viral clearance, and their role in inflammation and tissue damage is well documented (reviewed in *Watanabe et al., 2019*; *La Gruta et al., 2007*). A favorable outcome requires a balance between immune-mediated protection and pathology, and the viral-immunological landscape that drives disease and the markers that distinguish mild from severe influenza are complex. This is particularly true in humans (*Tang et al., 2019*) where obtaining high quality data from the lung is challenging, and viral loads in the upper respiratory tract do not always reflect the lower respiratory tract environment (*Feikin et al., 2017*; *Ai et al., 2020*; *Wong et al., 2020*; *Li et al., 2012*; *Ruuskanen et al., 2011*).

The accumulation of damage to the epithelium during IAV infection, either from virally-induced cell lysis or immune-mediated effects, is relatively understudied. We and others have modeled the lung damage and inflammation inflicted during pulmonary infections (e.g., as in *Smith et al., 2011b*; *Reynolds et al., 2006*; *Dunster et al., 2014*; *Ramirez-Zuniga et al., 2019*; *Baral et al., 2019*) but did so without sufficient data to constrain the model formulations. The difficulty in measuring the dynamics of infected cells and in establishing how damage correlates to specific host responses has been the primary impediment. However, recent technological advances, including the use of

reporter viruses (*Manicassamy et al., 2010*; *Tran et al., 2013*; *Karlsson et al., 2015*; *Luker and Luker, 2010*) and lung histomorphometry (*Marathe et al., 2016*; *Marathe et al., 2017*; *Sartorius et al., 2007*; *Zachariadis et al., 2006*; *Boyd et al., 2020*) within animal models, have provided an opportunity to acquire these types of measurements. Whole lung histomorphometry, which is broadly defined as a quantitative microscopic measurement of tissue shape, has recently increased in use due to the ability to directly stain, visualize, and quantify areas of infected cells. Even with these techniques, quantitative data over the course of infection is not currently available. Having data such as these should help reconcile potential nonlinearities in infected cell clearance and provide insight into the accumulated lung inflammation and damage, which are generally thought to be markers of disease severity. In addition, it should bolster the development of robust, predictive computational models, which have historically lacked constraint to these types of data.

In general, disease severity may not be directly correlated to viral loads or specific immunological components. In humans infected with IAV, viral loads typically increase prior to the onset of systemic symptoms, which peak around 2–3 d post-infection (pi) (*Carrat et al., 2008*; *Lee and Lee, 2010*; *Han et al., 2018*). Some symptoms (e.g., fever) are cytokine mediated (*Monto et al., 2000*), but respiratory symptoms often last longer and can remain following viral clearance (*Lee and Lee, 2010*; *Eccles, 2005*). This is particularly true when there is scarring of the lung tissue (*Li et al., 2012*). In the murine model, weight loss is used as an indicator of disease progression and severity, where greater weight loss corresponds to more severe disease (*Trammell and Toth, 2011*; *Bouvier and Lowen, 2010*; *Parzych et al., 2013*). Animal weights generally drop slowly in the first several days during an IAV infection and more rapidly as the infection begins to resolve (*Srivastava et al., 2009*; *Huang et al., 2017*). This is unlike viral load dynamics in these animals, which increase rapidly during the first 0–3 d pi then remain relatively constant prior to resolution (*Smith et al., 2018*). Because weight loss can occur following resolution of the infection, immune-mediated pathology is thought to play a role (*Lauder et al., 2011*; *Xu et al., 2004*; *Ostler et al., 2002*; *Parzych et al., 2013*; *Duan and Thomas, 2016*). Host and pathogen factors, such as age, viral proteins, and inoculum size, have also been shown to influence disease progression (*Toapanta and Ross, 2009*; *Lu et al., 2018*; *Smith et al., 2019*; *McAuley et al., 2007*). While the precise contribution of different factors to IAV-associated disease and mortality remain elusive, having tools that can link these with disease severity and decipher correlation from causation would improve our ability to effectively predict, understand, and treat the disease.

To gain deeper insight into the dynamics of viral resolution during primary pulmonary influenza infection and investigate the connection between viral loads, damage, inflammation, and disease severity, we developed and validated a mathematical model that describes viral kinetics and $CD8^+$ T cell-mediated infected cell clearance. The model accurately predicted the dynamics of effector and memory $CD8^+$ phenotypes, agreed with our previous results that infected cells are cleared in a density-dependent manner with CD8 efficiency rapidly accelerating by over 48,000 times in 2 d, and illuminated tradeoffs between the innate and adaptive immune responses. Our model predicted that infection duration is dependent on the magnitude of $CD8^+$ T cells rather than their efficacy, which we verified by depleting $CD8^+$ T cells. Quantitative whole lung histomorphometry showed that infected areas increase during the first 6 d of infection before clearing rapidly, that the relative number of $CD8^+$ T cells corresponded to the cleared area, and corroborated the model-predicted infected cell dynamics. These data also showed that the infection-induced lung injury is distinct from inflammation, and that each correlates to different immune responses and could be predicted using independent mathematical equations. In addition, the data revealed nonlinear connections between these two pathological measurements and disease severity. Together, our data, model, and analyses provide a robust quantification of the density-dependent nature of $CD8^+$ T cell-mediated clearance, and the critical connections between these cells and the dynamics of viral loads, infected cells, lung injury, inflammation, and disease severity.

Results

Virus and $CD8^+$ T cell kinetics

In animals infected with 75 $TCID_{50}$ PR8, virus rapidly infects cells or is cleared within 4 hr pi and is undetectable in all animals at this time (*Figure 1*). Virus then increases exponentially and peaks after
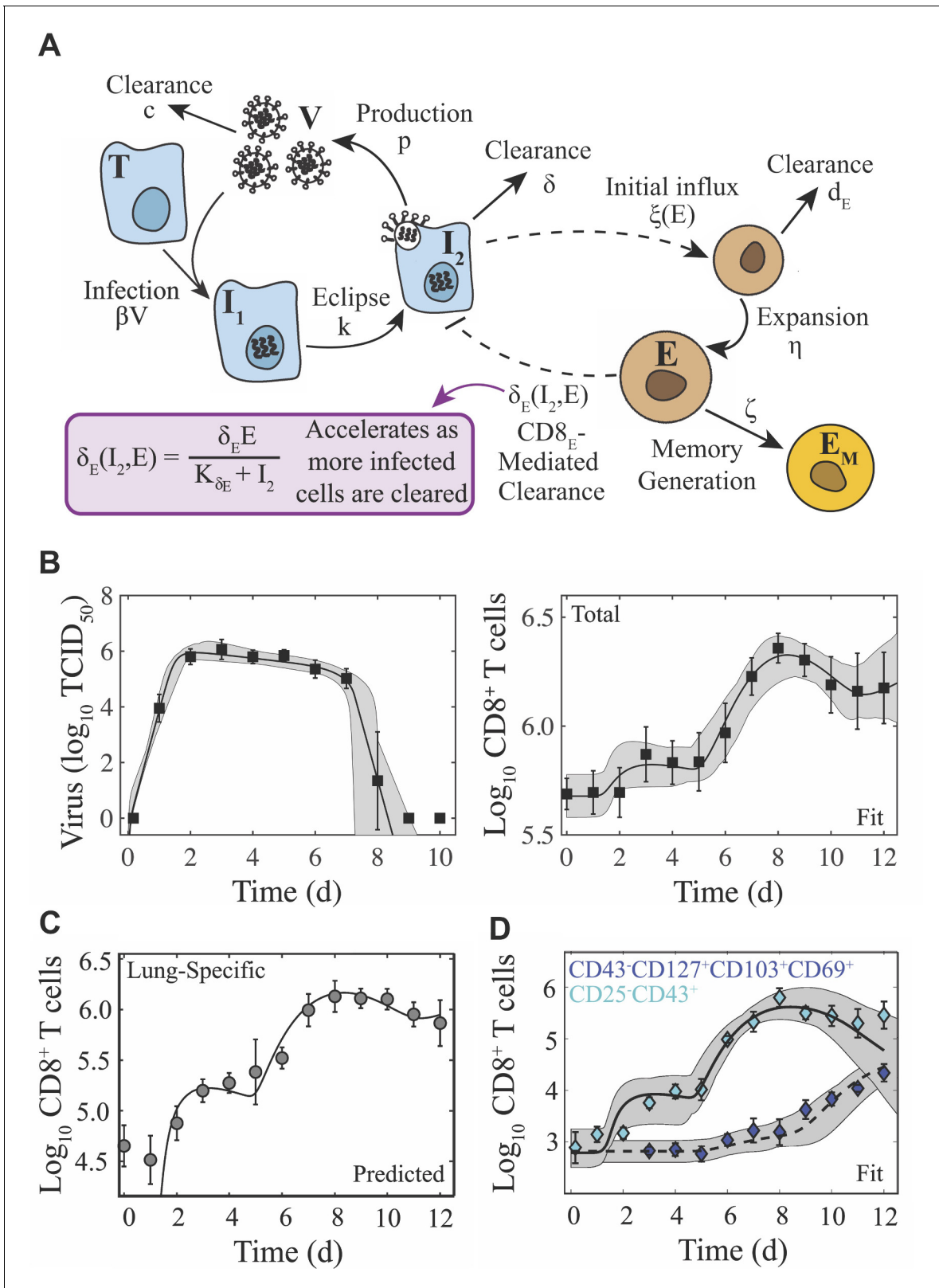
Figure 1. Schematic and fit of the CD8^{+} T cell viral kinetic model. (**A**) Schematic of the CD8^{+} T cell model in *Equation (1)-(6)*. In the model, target cells (T) are infected at rate βV. Infected cells (I_1) undergo an eclipse phase and transition to become productively-infected cells (I_2) at rate k. Virus (V) is produced by infected cells at rate p and is cleared at rate c. Infected cells are cleared at rate δ by non-specific mechanisms and at rate $\delta_E(I_2, E)$ by effector CD8^{+} T cells (E; denoted CD8$_E$). The dashed lines represent interactions between infected cells and CD8$_E$. Initial CD8$_E$ influx

Figure 1 continued on next page

Figure 1 continued

($\xi(E) = \xi/(K_E + E)$) is proportional to infected cells and is limited by $CD8_E$ with half-saturation constant K_E. $CD8_E$ expansion (η) occurs proportional to infected cells τ_E days ago. Memory $CD8^+$ T cell (E_M; denoted $CD8_M$) generation occurs at rate ζ and proportional to $CD8_E$ τ_M days ago. **(B)** Fit of the $CD8^+$ T cell model (*Equation (1)-(6)*) to virus and total $CD8^+$ T cells from the lungs of mice infected with 75 $TCID_{50}$ PR8 (10 mice per time point). The total number of $CD8^+$ T cells is $\hat{E} = E + E_M + \hat{E}_0$. **(C)** Total $CD8^+$ T cells in the lung parenchyma (gray circles) and overlay of the model predicted values ($E + E_M$). **(D)** Fit of the model to virus, $CD25^-CD43^+$ $CD8^+$ T cells (cyan diamonds; E), and $CD43^-CD127^+CD103^+CD69^+$ $CD8^+$ T cells (blue diamonds; E_M) (five mice per time point). The solid and dashed black lines are the optimal solutions and the gray shading is are the model solutions using parameter sets within the 95% CIs. Parameters are given in *Table 1*. Data are shown as mean ± standard deviation.

The online version of this article includes the following figure supplement(s) for figure 1:

Figure supplement 1. Dynamics of $CD8^+$ T cells in the lung parenchyma and vasculature.
Figure supplement 2. Flow cytometry gating strategy for $CD8^+$ T cell analysis.

~2 d pi. Following the peak, virus enters a biphasic decline. In the first phase (2–6 d pi), virus decays slowly and at a relatively constant rate (0.2 $\log_{10}$ $TCID_{50}$/d) (*Smith et al., 2018*). In the second phase (7–8 d pi), virus is cleared rapidly with a loss of 4–5 $\log_{10}$ $TCID_{50}$ in 1–2 d (average of –3.8 $\log_{10}$ $TCID_{50}$/d) (*Smith et al., 2018*). $CD8^+$ T cells remain at their baseline level from 0–2 d pi, where ~15% are located in the circulating blood, ~75% in the lung vasculature, and ~10% in the lung parenchyma (*Figure 1—figure supplement 1*) with the majority in the lung as $CD43^-CD127^+$. IAV-specific $CD8^+$ T cells that are recently primed ($CD25^+CD43^+$) or effector cells ($CD25^-CD43^+$) (*Keating et al., 2018*) begin appearing in the lung and increase slightly from 2– 3 d pi but remain at low levels. These cells are thought to proliferate within the lung at least once by 4 d pi (*McGill and Legge, 2009*), and their populations briefly contract (3–5 d pi) before expanding rapidly (5–8 d pi). During the expansion phase, >95% of recovered cells are in the lung (~70% in the parenchyma and ~30% in the vasculature) with $CD25^+CD43^+$ and $CD25^-CD43^+$ as the predominant phenotypes. This is in accordance with prior studies that showed these phenotypes are IAV-specific and that their expansion dynamics in the lung were not altered by removing blood-borne $CD8^+$ T cells from the analysis (*Anderson et al., 2012*; *Keating et al., 2018*).

$CD8^+$ T cell expansion corresponds to the second viral decay phase with sixty percent of mice clearing the infection by 8 d pi and the other forty percent by 9 d pi (*Figure 1*). Most $CD43^+CD8^+$ T cell phenotypes decline following viral clearance (8–10 d pi) but do not return to their baseline level by 12 d pi. Long-lived antigen-specific memory phenotypes down regulate CD43 (*Jones et al., 1994*; *Harrington et al., 2000*; *Onami et al., 2002*) and gradually increase substantially beginning at 9 d pi with most as $CD25^-$, which is qualitatively similar to other studies (*Harrington et al., 2000*). At 12 d pi, ~55% of $CD8^+$ T cells remain in the lung parenchyma and ~20% in the circulating blood indicating exit from the lung (*Figure 1—figure supplement 1*).

Viral kinetic model with density-dependent $CD8^+$ T cell-mediated clearance

We previously described the influenza viral load kinetics and biphasic decline during primary pulmonary infection using a density-dependent (DD) model (*Smith et al., 2018*), which assumes that the rate of infected cell clearance increases as the density of infected cells decreases (i.e., $\delta_d(I_2) = \delta_d/(K_\delta + I_2)$). Because the rapid decay of virus is thought to be due to the clearance of infected cells by $CD8^+$ T cells, it is unknown if early $CD8^+$ T cell presence contributes to infected cell clearance, and no model has captured the entire $CD8^+$ T cell time course, we developed a model that describes the dynamics of these cells and their efficiency in resolving the infection (*Equation (1)-(6)*; *Figure 1A*). The model includes equations for effector (E, denoted $CD8_E$) and memory (E_M, denoted $CD8_M$) $CD8^+$ T cells, and two mechanisms of infected cell clearance. The first mechanism is from unspecified, innate mechanisms, which is relatively constant (δ) and primarily acts during the first viral decay phase (2–6 d pi). The second is the $CD8_E$-mediated infected cell clearance, which occurs at a rate that increases as the density of infected cells decreases ($\delta_E(I_2,E) = \delta_E E/(K_{\delta_E} + I_2)$) and primarily acts during the rapid, second viral decay phase (7–8 d pi). Excluding this density dependence entirely resulted in a significant and premature decline in viral loads, which disagreed with the experimental data. We also tested whether the density dependence could be included in the $CD8^+$ T cell expansion rate rather than in the infected cell clearance rate (see Appendix 1) as other models have done (e.g., as in *Baral et al., 2019*; *Bonhoeffer et al., 2000*; *Conway and*

Perelson, 2015). This modification yielded a close fit to the CD8$^+$ T cell data at 6–10 d pi but not at the early time points (*Appendix 1—figure 1*). In addition, the viral load data was underestimated at 7 d pi causing the solution to miss the rapid decline between 7–8 d pi and result in a statistically poorer fit. Thus, retaining the density-dependence in the rate of infected cell clearance most accurately captured the entire dataset. The model includes terms for the initial CD8$_E$ influx at 2–3 d pi ($\xi I_2/(K_E + E)$) and for CD8$_E$ expansion ($\eta E I_2(t - \tau_E)$), which accounts for the larger increase between 5–8 d pi. To capture the contraction of CD8$^+$ T cells between these times (3–5 d pi), it was necessary to assume that the initial CD8$_E$ influx is regulated by their own population (i.e., $\xi(E) = \xi/(K_E + E)$). In both terms, the increase is proportional to the number of infected cells. Although memory CD8$^+$ T cells were not the primary focus here, it was necessary to include the CD8$_M$ population because CD8$^+$ T cells are at a significantly higher level at 10–12 d pi than at 0 d pi (*Figure 1B*). Fitting the model simultaneously to viral loads and total CD8$^+$ T cells from the (non-perfused) lungs of infected animals illustrated the accuracy of the model (*Figure 1B*). The resulting parameter values, 95% confidence intervals (CIs), ensembles, and histograms are given in *Table 1*, *Figure 2*, and *Figure 2—figure supplements 1–2*.

Plotting the model predicted dynamics for the lung-specific CD8$^+$ T cells ($\text{CD8}_L = E + E_M$) illustrated the accuracy of the model in predicting their dynamics within the lung parenchyma without fitting to these data (*Figure 1C*). One benefit of using the total CD8$^+$ T cells is that the model

Table 1. CD8$^+$ T cell model parameters.

Parameters and 95% confidence intervals obtained from fitting the CD8$^+$ T cell model (*Equation (1)-(6)*) to viral titers and total CD8$^+$ T cells ('Total CD8') or viral titers, CD25$^-$CD43$^+$CD8$^+$ T cells, and CD43$^-$CD127$^+$CD103$^+$CD69$^+$CD8$^+$ T cells ('Specific CD8$_{E,M}$ Phenotypes') from mice infected with 75 TCID$_{50}$ PR8. CD8$_E$ and CD8$_M$ denote effector (E) and memory (E_M) CD8$^+$ T cells, respectively. The total number of CD8$^+$ T cells is $\hat{E} = E + E_M + \hat{E}_0$ and is denoted by CD8.

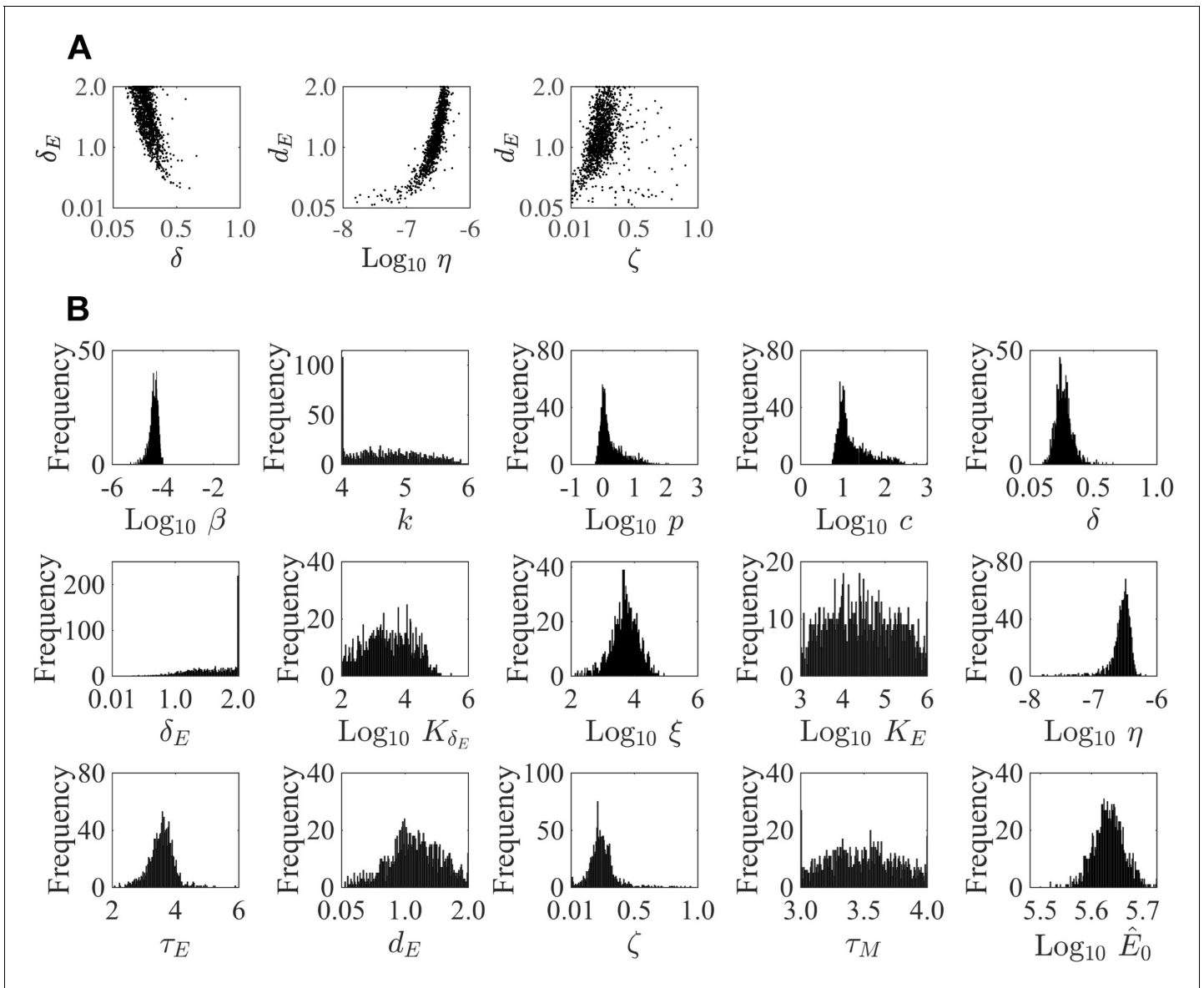| Parameter	Description	Units	Total CD8		Specific CD8$_{E,M}$ phenotypes	
			Value	95% CI	Value	95% CI
β	Virus infectivity	TCID$_{50}^{-1}$ d^{-1}	6.2×10^{-5}	[5.3×10^{-6}, 1.0×10^{-4}]	3.7×10^{-5}	[1.1×10^{-5}, 9.4×10^{-5}]
k	Eclipse phase transition	d^{-1}	4.0	[4.0, 6.0]	5.1	[4.0, 6.0]
p	Virus production	TCID$_{50}$ cell^{-1} d^{-1}	1.0	[$5.8 \times 10^{-1} \times 1.1 \times 10^2$]	1.5	[0.73, 13.6]
c	Virus clearance	d^{-1}	9.4	[5.6, 9.5×10^2]	12.1	[5.8, 17.5]
δ	Infected cell clearance	d^{-1}	2.4×10^{-1}	[1.0×10^{-1}, 6.6×10^{-1}]	3.0×10^{-1}	[1.9×10^{-1}, 5.9×10^{-1}]
δ_E	Infected cell clearance by CD8$_E$	cells CD8$_E^{-1}$ d^{-1}	1.9	[$3.3. \times 10^{-1}$, 2.0]	5.7	[1.7, 8.5]
K_{δ_E}	Half-saturation constant	cells	4.3×10^2	[1.0×10^2, 2.9×10^5]	1.3×10^2	[1.0×10^1, 8.6×10^2]
ξ	CD8$_E$ infiltration	CD8$_E^2$ cell^{-1} d^{-1}	2.6×10^4	[1.3×10^2, 8.7×10^4]	2.9×10^3	[8.0×10^2, 1.7×10^4]
K_E	Half-saturation constant	CD8$_E$	8.1×10^5	[1.0×10^3, 1.0×10^6]	2.2×10^6	[1.1×10^6, 8.3×10^6]
η	CD8$_E$ expansion	cell^{-1} d^{-1}	2.5×10^{-7}	[1.6×10^{-8}, 6.7×10^{-7}]	3.5×10^{-7}	[2.3×10^{-7}, 5.2×10^{-7}]
τ_E	Delay in CD8$_E$ expansion	d	3.6	[2.1, 5.9]	3.3	[2.6, 3.8]
d_E	CD8$_E$ clearance	d^{-1}	1.0	[5.1×10^{-2}, 2.0]	1.1	[3.3×10^{-1}, 2.5]
ζ	CD8$_M$ generation	CD8$_M$ CD8$_E^{-1}$ d^{-1}	2.2×10^{-1}	[1.0×10^{-2}, 9.4×10^{-1}]	3.2×10^{-2}	[1.0×10^{-2}, 2.2×10^{-1}]
τ_M	Delay in CD8$_M$ generation	d	3.5	[3.0, 4.0]	3.3	[2.1, 5.3]
$\hat{E}_0$	Baseline CD8 or CD8$_E$	CD8 or CD8$_E$	4.2×10^5	[$3.3. \times 10^5$, 5.3×10^5]	6.0×10^2	[3.1×10^2, 1.8×10^2]
$\hat{E}_{M0}$	Baseline CD8$_M$	CD8$_M$	-	-	6.5×10^2	[3.2×10^2, 1.5×10^3]
$T(0)$	Initial uninfected cells	cells	1×10^7	-	1×10^7	-
$I_1(0)$	Initial infected cells	cells	75	-	75	-
$I_2(0)$	Initial infected cells	cells	0	-	0	-
$V(0)$	Initial virus	TCID$_{50}$	0	-	0	-
$E(0)$	Initial CD8$_E$	CD8$_E$	0	-	0	-
$E_M(0)$	Initial CD8$_M$	CD8$_M$	0	-	0	-

Figure 2. Parameter ensembles and histograms. Parameter ensembles (A) and histograms (B) resulting from fitting the CD8+ T cell viral kinetic model (*Equation (1)-(6)*) to viral titers and total CD8+ T cells from mice infected with 75 TCID$_{50}$ PR8. (A) The rates of infected cell clearance by non-specific mechanisms (δ) and by CD8$_E$ (δ_E) are slightly negatively correlated. Correlations were also present between the rates of CD8$_E$ clearance (d_E), CD8$_E$ expansion (η), and CD8$_M$ generation (ζ). The axes limits reflect imposed bounds. Additional ensemble plots are in *Figure 2—figure supplements 1–2*. (B) The histograms show that the majority of parameters are well-defined with the exception of the eclipse phase transition rate (k), one of the half-saturation constants (K_E), and the CD8$_M$ generation delay (τ_M).

The online version of this article includes the following figure supplement(s) for figure 2:

Figure supplement 1. Parameter ensembles.
Figure supplement 2. Parameter ensembles.

automatically deduces the dynamics of effector-mediated killing and memory generation without needing to specify which phenotypes might be involved in these processes as they may be dynamically changing. However, the rates of expansion, contraction, and infected cell clearance may be different if only certain phenotypes are engaged. Thus, we examined whether the model could fit the dynamics of the predominant effector (CD25−CD43+) and memory (CD43−CD127+CD103+CD69+) phenotypes. Re-fitting the model to these data suggested that no changes to model formulation

were needed and there were only small alterations to select CD8-specific parameter values (*Figure 1D*; *Table 1*).

Plotting the model ensembles revealed a correlation between the two infected cell clearance parameters (δ and δ_E; *Figure 2B*), which represent the efficacy of the non-specific immune response and the CD8$^+$ T cell response, respectively. Performing a sensitivity analysis showed that the viral load dynamics do not change substantially when these parameters are increased or decreased (*Appendix 2—figure 1*) . However, decreasing the rate of non-specific infected cell clearance (i.e., lower δ) resulted in a significant increase in the number of CD8$_E$ due to the small increase in the number of infected cells (*Figure 1*). Even with a larger CD8$_E$ population, recovery was delayed by only ~0.1 d. Given the correlation between δ and δ_E (*Figure 2B*), a more efficient CD8$_E$ response (i. e., higher δ_E) may be able to overcome this short delay in resolution. The lack of sensitivity to changes in the infected cell clearance parameters is in contrast to the DD model, where the viral dynamics were most sensitive to perturbations in δ_d (*Appendix 2—figure 1*; *Smith et al., 2018*), which encompasses multiple processes. With CD8$^+$ T cells explicitly included in the model, the infection duration was most sensitive to changes in the rate of CD8$_E$ expansion (η) (*Figure 1*, *Appendix 1—figure 1*; discussed in more detail below).

Examining the parameter ensembles and sensitivity analysis also yielded insight into how other model parameters affect the CD8$^+$ T cell response. The rates of CD8$_E$ expansion (η) and clearance (d_E) were slightly correlated, indicating a balance between these two processes (*Figure 2A*). This correlation and the sensitivity of η produced model dynamics that were also sensitive to changes in the CD8$_E$ clearance rate (d_E) (*Appendix 3—figure 2*). As expected, the rates of CD8$_M$ generation (ζ) and CD8$_E$ clearance (d_E) were correlated (*Figure 2A*). It has been estimated that approximately 5–10% of effector CD8$^+$ T cells survive to become a long-lasting memory population (*Kaech et al., 2002*). Despite the inability to distinguish between CD8$_E$ and CD8$_M$ in the total CD8$^+$ T cell data, the model predicts that 17% of CD8$_E$ transitioned to a memory class by 15 d pi. When considering only the CD25$^-$CD43$^{+/-}$ effector and memory phenotypes, the model estimates this value to be ~7%. Additional insight into the regulation of the CD8$^+$ T cell response, results from the model fitting, and a comparison of the DD model and the CD8$^+$ T cell model are included in Appendix 2.

Density-dependent infected cell clearance

Given the accuracy of the model, we next sought to gain further insight into the nonlinear dynamics of CD8$^+$ T cell-mediated infected cell clearance. Plotting the clearance rate ($\delta_E(I_2, E) = \delta_E E/(K_{\delta_E} + I_2)$) as a function of infected cells (I_2) and CD8$_E$ (E) (*Figure 3*) confirmed that there is minimal contribution from CD8$_E$-mediated clearance to viral load kinetics or infected cell kinetics prior to 7 d pi (*Figure 3A–C*, markers a–b). At the initiation of the second decay phase (7 d pi), the clearance rate is $\delta_E(I_2, E) = 3.5/\text{d}$ (*Figure 3A–B*, marker c). As the infected cell density declines toward the half-saturation constant ($K_{\delta_E} = 4.3 \times 10^2 \text{ cells}$), the clearance rate increases rapidly to a maximum of 4830/d (*Figure 3A–C*, markers d–g). The model predicts that there are 6×10^5 infected cells remaining at 7 d pi, which can be eliminated by CD8$_E$ in 6.7 h.

To explore how recovery time is altered by varying CD8$_E$ levels, we examined the resulting dynamics from increasing or decreasing the rate of CD8$_E$ expansion (η). When η was increased by 50%, the CD8$_E$ population increased by a substantial 670% (*Appendix 3—figure 1*). However, this was insufficient to significantly shorten the infection (8.4 d versus 7.8 d). The infection duration could be reduced if CD8$_E$ expansion began earlier (i.e., smaller τ_E; *Appendix 3—figure 2*). Although recovery is not significantly expedited by a larger CD8$_E$ population, our model predicted that the infection would be dramatically prolonged if these cells are sufficiently depleted (*Figure 3D–E* and *Figure 1*). This *in silico* analysis revealed a bifurcation in recovery time, such that the infection is either resolved within ~15 d pi or may last up to ~45 d if CD8$_E$ are below a critical magnitude required to resolve the infection (*Figure 3D–E*). The critical number of total CD8$^+$ T cells needed for successful viral clearance was $\hat{E}_{\max}^{\text{crit}} = 7.4 \times 10^5$ CD8, which was 39.2% of the maximum number of CD8$^+$ T cells obtained from the best-fit solution (i.e., $\hat{E}_{\max} = 1.9 \times 10^6$ CD8). This corresponds to 17% of CD8$_E$ (i.e., $E_{\max}^{\text{crit}} = 2.3 \times 10^5$ CD8$_E$; *Figure 3D–E*). The model analysis indicated that decreasing the total number of CD8$^+$ T cells by as little as 0.1% from this critical level (i.e., 39.2% to 39.1%) lengthened the infection from 15 d pi to 25 d pi (*Figure 3D*).
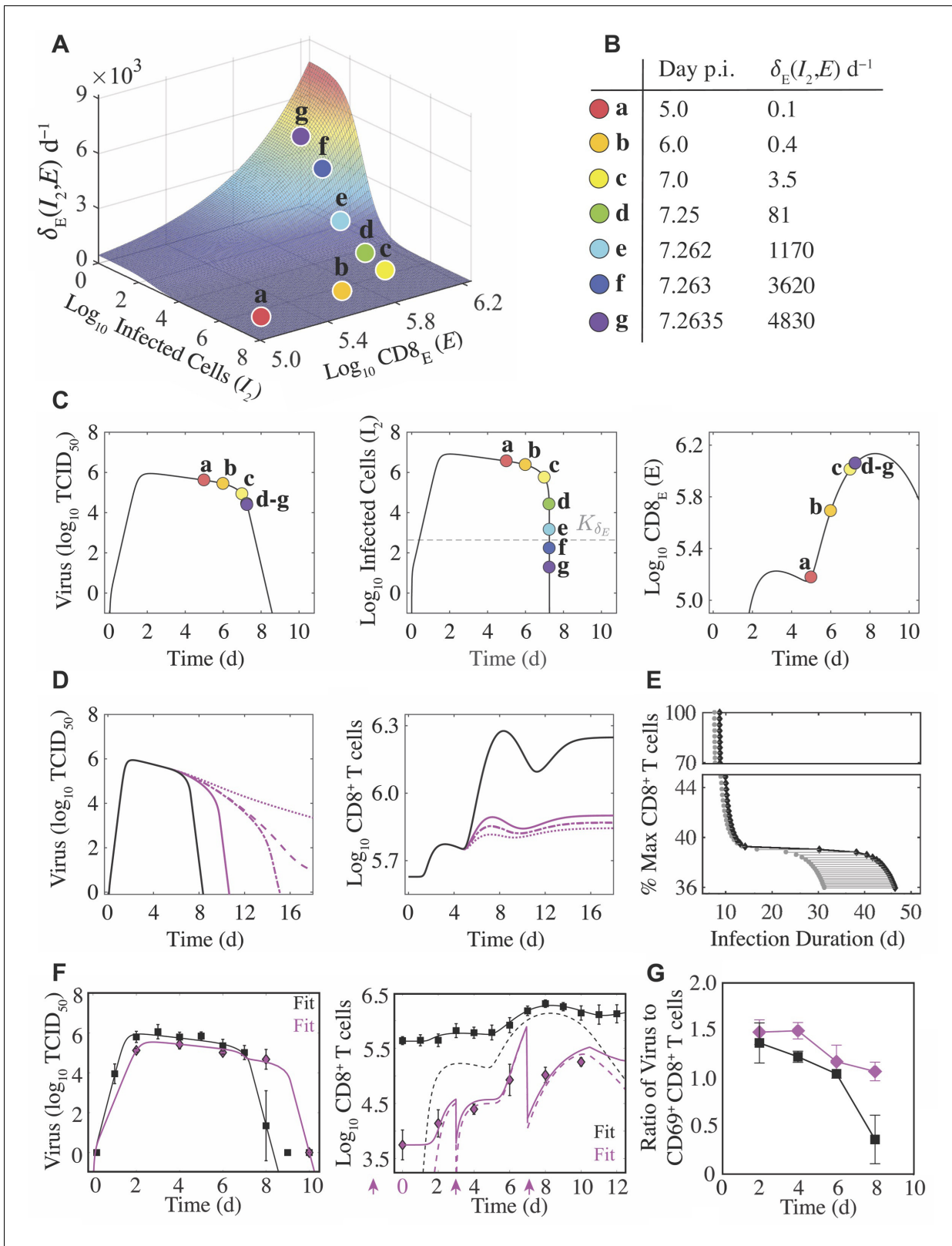
Figure 3. Density-dependent infected cell clearance by CD8+ T cells and their impact on recovery time. (A) The rate of CD8$_E$-mediated infected cell clearance ($\delta_E(I_2, E) = \delta_E E/(K_{\delta_E} + I_2)$) plotted as a function of infected cells (I_2) and effector CD8+ T cells (E; CD8$_E$). The colored markers (denoted a–g) indicate the infected cell clearance rate that corresponds to different time points during the infection for the best-fit solution. (B) Values of $\delta_E(I_2, E)$ for the indicated time points associated with the markers a–g. (C) Corresponding locations of the various $\delta_E(I_2, E)$ values (markers a–g) on the best-fit

Figure 3 continued on next page

solution of the CD8$^+$ T cell model for virus (V), infected cells (I_2), and CD8$_E$ (E). (D) Solutions of the CD8$^+$ T cell model (*Equation (1)-(6)*) for virus (V) and total CD8$^+$ T cells ($\hat{E}$) using the best-fit parameters (black line) and when varying the CD8$_E$ expansion rate (η; magenta lines) to illustrate how different total CD8$^+$ T cell magnitudes alter infection duration. The magenta lines are solutions from when the percent $\hat{E}_{max}$ relative to $\hat{E}_{max}$ from the best-fit solution was 42% (solid line), 39.2% (dash-dotted line), 39.1% (dashed line), or 37% (dotted line). (E) The time at which infected cells reach the half-saturation constant ($I_2 = K_{\delta_E}$; gray circles) and the infection duration (time where $\log_{10} V = 0$; black diamonds) are shown for the various CD8$^+$ T cell magnitudes. The gray line between these points is the time required to eliminate K_{δ_E} infected cells and achieve complete resolution of the infection ($\log_{10} V = 0$). (F) Fit of the CD8$^+$ T cell model (*Equation (1)-(6)*) to viral loads and CD8$^+$ T cells (magenta diamonds) following depletion at -2, 0, 3, and 7 d pi (magenta arrows). The best model (*Supplementary file 2*) resulted in fewer target cells (T_0), a lower CD8$_E$ influx (ξ), and a higher CD8$_E$ expansion rate (η). All other parameters were fixed to the best-fit value in *Table 1*. The solid lines are $\hat{E} = E + E_M + \hat{E}_0$ and the dashed lines are E for the cases where CD8$^+$ T cells were depleted (magenta) and where they were not depleted (black). (G) Comparison of the $\log_{10}$ ratio of virus to CD69$^+$CD8$^+$ T cells with and without CD8$^+$ T cell depletion (magenta and black, respectively). All data are shown as mean ± standard deviation.

Dynamical changes during CD8$^+$ T cell depletion

To further test our model formulation and identify how viral load kinetics are altered with dynamically changing CD8$^+$ T cells, we infected groups of mice with 75 TCID$_{50}$ and depleted these cells at -2 d, 0 d, 3 d, and 7 d pi with an anti-CD8α antibody (clone 2.43; *Figure 3F*). CD8$^+$ T cells were reduced with over 99% efficiency and only 1.3% remained 2 d after depletion in the absence of infection (i.e., at 0 d pi; *Figure 3F*). CD8$^+$ T cells remained >1 log$_{10}$ lower throughout the infection. Unexpectedly, the corresponding viral loads were significantly lower at 2 d pi (p=0.02) and consistently lower at other time points early in the infection (4 d pi (p=0.1) and 6 d pi (p=0.2)). As expected and predicted by our mathematical model, viral loads were significantly higher at 8 d pi (4.68 log$_{10}$ TCID$_{50}$ compared to 1.42 log$_{10}$ TCID$_{50}$; p=0.01). By 10 d pi, a sufficient number of CD8$^+$ T cells were present and all animals had cleared the infection (*Figure 3F*). Interestingly, the number of CD8$^+$ T cells at 10 d pi was only slightly higher than at 8 d pi (5.25 log$_{10}$ versus 5.02 log$_{10}$; p=0.064) further highlighting the density-dependent dynamics described above.

Given that viral loads were lower at early time points and that the anti-CD8α antibody is known to cause concentration-dependent changes in CD8$_E$ differentiation, activation, and efficacy (*Cross et al., 2019*) in addition to resulting in death of the cells that would initiate activation of and removal by other immune cells, we did not expect our model to match the data without modulation of parameter values. However, we did expect that no changes to the model formulation would be required. In total, we tested >30 'models' where 1–4 parameters were altered and found one model that was significantly better according to the AIC (*Supplementary file 1*). In that model, the initial number of target cells (T_0) was 2.5x lower (~4×10^6 versus 1×10^7 cells), the rate of initial CD8$_E$ influx (ξ) was 2x lower (1.3×10^4 versus 2.6×10^4 CD8$_E^2$ cell^{-1} d^{-1}), and the rate of CD8$_E$ expansion (η) was 4x higher (1×10^{-6} versus 2.5×10^{-7} cell^{-1} d^{-1}). The second best model had a lower cost but was penalized by an additional parameter. That model suggested similar results but replaced the effect on T_0 with a combination of a lower virus production rate (p) and higher non-specific infected cell clearance rate (δ). Both models resulted in fewer infected cells and, thus, have approximately equivalent interpretations.

To further examine these findings, we plotted the ratio of virus to activated (CD69$^+$) CD8$^+$ T cells (*Figure 3G*). At 2 d pi, the ratio was similar for the depleted and mock-treated groups (p=0.41) suggesting that the depletion-induced reduction in virus was proportional to the reduction in activated CD8$^+$ T cells. However, at 4 d pi, the ratio in the depleted groups was significantly higher (p=0.0028) for otherwise similar levels of virus. This signifies that there were disproportionately low numbers of CD8$^+$ T cells and, thus, reduced influx (i.e., lower ξ). By 6 d pi, the ratios were again similar (p=0.25) implying a higher expansion of these cells (i.e., higher η). Investigation into the predicted target cell reduction is included below.

Modeling lung injury dynamics

To investigate the dynamics of infected cells and their clearance by CD8$^+$ T cells, we quantified these cells and the progression and resolution of lung injury using serial whole lung histomorphometry (*Figure 4A*). Antigen-positive areas of the lung ('active' lesions) were first detectable at 2 d pi (*Figure 4A–B*), which coincides with the peak in viral loads. The infected area continued to increase
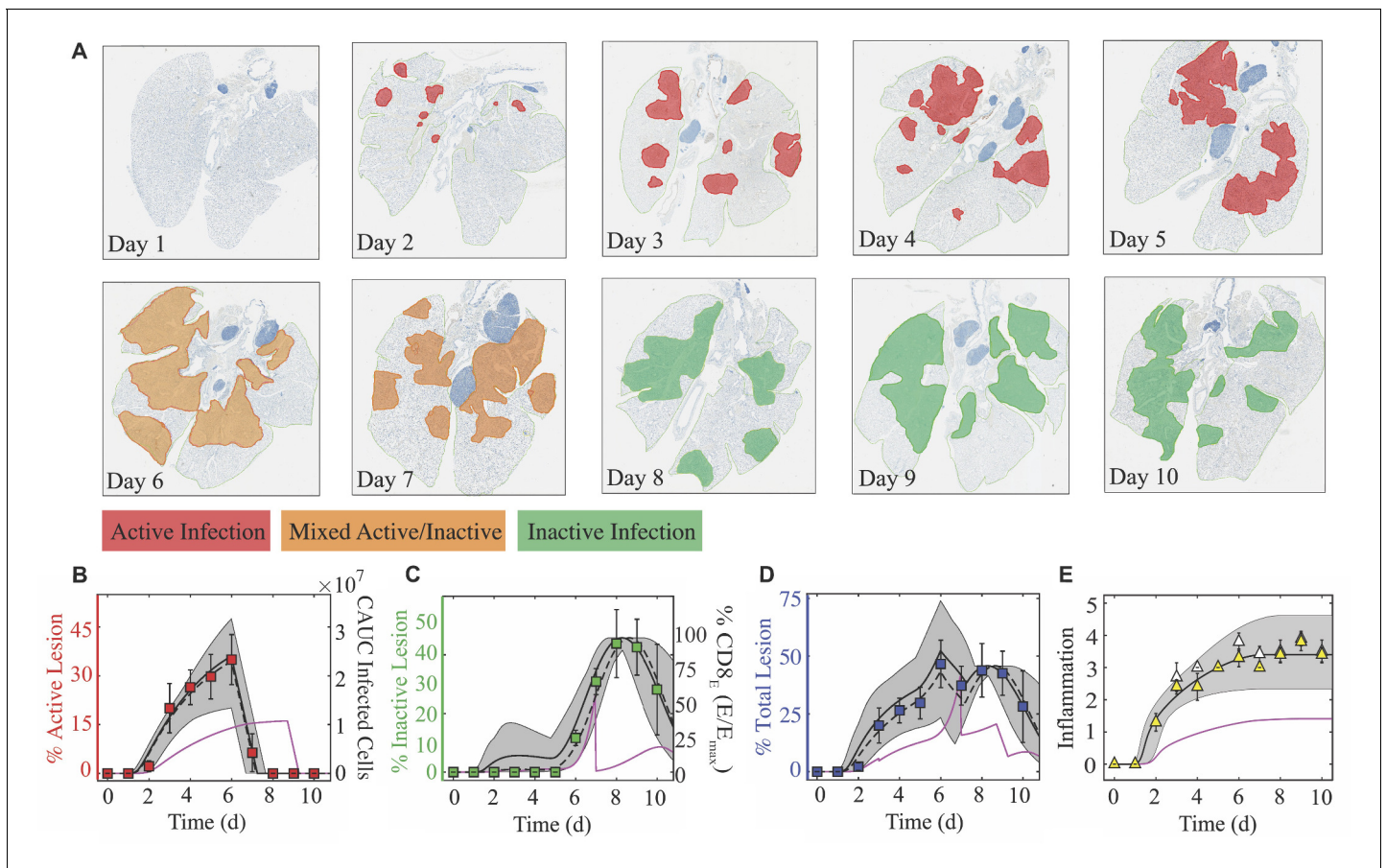
Figure 4. Histomorphometry and inflammation of the IAV-infected lung. (**A**) Whole lung sections with histomorphometry showing the areas of influenza NP-positive 'active' lesions (red), previously infected 'inactive' lesions with minimal antigen-positive debris (green), or mixed active and inactive regions (orange) throughout the infection. Representative images from each group are shown. (**B**) Percent active lesion (red squares) plotted together with the cumulative area under the curve (CAUC) of the predicted infected cell dynamics (I_2) obtained from fitting the CD8$^+$ T cell model. The linear decline in the active lesion ($-28.7\%/d$; see **Figure 4—figure supplement 1**) was used to estimate the decline after 6 d pi. (**C**) Percent inactive lesion (green squares) plotted together with the percent maximum CD8$_E$ (E/E_{max}) obtained from fitting the CD8$^+$ T cell model. (**D**) The total lesion (blue squares) is the addition of the active and inactive lesions. To include all measurements on the same scale, the CAUC of I_2 was multiplied by a scaling factor of 14.2% per 1×10^7 cells, and the percent maximum CD8$_E$ was multiplied by a scaling factor of 0.46%. (**E**) Fit of **Equation (7)** to the alveolar (white triangles) and interstitial (yellow triangles) inflammation scores. The solid black, dashed black, and solid magenta lines are the curves generated using the best-fit parameters obtained from fitting the model to the total CD8$^+$ T cells, the CD25$^-$CD43$^+$ and CD43$^-$CD127$^+$CD103$^+$CD69$^+$ CD8$^+$ T cells, and the total CD8$^+$ T cells during CD8 depletion, respectively. The gray shading are the curves generated using the 95% CI parameters from fitting the model to the total CD8$^+$ T cells. All data are shown as mean ± standard deviation.

The online version of this article includes the following figure supplement(s) for figure 4:

Figure supplement 1. Regression analysis of lung injury dynamics and CD8$^+$ T cells.

Figure supplement 2. Correlation of inflammation with macrophages and neutrophils.

in a nonlinear manner until 6 d pi, whereas viral loads remained high until 7 d pi (**Figure 1B**). At this time, resolution of the infection began and the infected area declined at a rate of ~28.7%/d between 6–7 d pi (**Figure 4—figure supplement 1**). Few to no infected cells were present at 8 d pi (**Figure 4A**). Correspondingly, virus was undetectable in most animals by 8 d pi (**Figure 1B**). Because the percent active lesion is a reflection of the influenza-positive cells, we examined whether the CD8$^+$ T cell model accurately predicted these dynamics. In the model, the accumulated infection is defined by the cumulative area under the curve (CAUC) of the productively infected cells (I_2). Plotting the percent active lesion against the CAUC of I_2 shows that the model accurately reflects the cumulative infected cell dynamics and, thus, the infection progression within the lung (**Figure 4B**). Plotting the CAUC of I_2 for all parameter sets in the 95% CIs and from fitting the model to specific

phenotypes further illustrates the accuracy by showing that the heterogeneity in the histomorphometry data is captured (*Figure 4B*), which is larger than the heterogeneity in viral loads (*Figure 1B*). Plotting the predicted active lesion dynamics for the model parameterized to the data where CD8$^+$ T cells were depleted suggested that there was a ~22% reduction in the active lesion (*Figure 4B*).

Antigen-negative, previously-infected or damaged areas of the lung ('inactive' lesions) are evident beginning at 5 d pi (*Figure 4A,C*). This resolution of the infection continued from 5-8 d pi, causing a 15.1%/d increase in the area of inactive lesions (*Figure 4—figure supplement 1*). Following this, healing of the injured lung is apparent as the inactive lesioned area declines (-14.5%/d from 9–10 d pi; *Figure 4C* and *Figure 4—figure supplement 1*). These dynamics generally parallel the CD8$^+$ T cell dynamics but are nonlinearly correlated (*Figure 4—figure supplement 1*). Fitting a line to the CD8$^+$ T cell data from 5-8 d pi indicated that the influx rate of all phenotypes is 4.94×10^5 cells/d, of lung-specific phenotypes is 3.97×10^5 cells/d, and of the CD25$^-$CD43$^+$ effector phenotype is 1.98×10^5 cells/d (*Figure 4—figure supplement 1*). Thus, the model estimates that, on average, every 100,000 total, lung-specific, or CD25$^-$CD43$^+$ CD8$^+$ T cells clear ~3.1%, ~3.8%, or ~7.6% of the infected areas within the lung, respectively. During the CD8$^+$ T cell contraction phase, a similar linear regression analysis suggested that these cells decline at rates of $\sim 4.13 \times 10^5$ CD8/d (total), $\sim 2.35 \times 10^4$ CD8/d (lung-specific), and $\sim 3.83 \times 10^4$ CD8/d (CD25$^-$CD43$^+$) (*Figure 4—figure supplement 1*). Similar to the relation discussed above, the dynamics of the damaged areas of the lung corresponded to the dynamics of the percent maximum CD8$_E$ (i.e., E/E_{max}) in the model (*Figure 4C*). Our model suggested a ~37% reduction in the inactive lesion during CD8$^+$ T cell depletion (*Figure 4C*). Adding the predicted dynamics for the active and inactive lesions agrees with the dynamics of the total lesion, but is slightly underestimated when using the model fit to CD25$^-$CD43$^+$ CD8$^+$ T cells (*Figure 4D*). In addition, the predicted total lesion was reduced for the case where CD8$^+$ T cells were depleted (*Figure 4D*).

Modeling lung inflammation dynamics

In addition to measuring virus-induced lung damage, lung inflammation was scored (*Figure 4E*). Both alveolar and interstitial inflammation begin to increase at 2 d pi with the sharpest increase between 1–3 d pi. Inflammation continues to increase until 6 d pi with a maximum score of 3.5–4.0 out of 5. Resolution of inflammation was not evident during the time course of our data, which concluded at 10 d pi. This is in contrast to the lung damage inflicted by the virus, which begins declining at 8 d pi and shows that ~15% of the damage was repaired by 10 d pi. Inflammation was linearly correlated to inflammatory macrophages and to neutrophils (*Figure 4—figure supplement 2*), which were excluded from the model. However, the knowledge that the model's predicted infected cell dynamics are accurate and that these cells can produce cytokines and chemokines that attract cells like macrophages and neutrophils suggested that our model could be used to estimate inflammation. To do this, we fit *Equation (7)* to the inflammation scores while keeping all other parameters fixed to their best-fit values (*Table 1*). The results suggested that the equation captured the inflammation dynamics, and that the contribution from the initial infected cell class (I_1) was $\alpha_1 = 4.27 \text{ per } 10^7 \text{ cells/d}$ and the contribution from the productively infected cells (I_2) was $\alpha_2 = 0.87 \text{ per } 10^7 \text{ cells/d}$. For the case where CD8$^+$ T cells were depleted, *Equation (7)* estimated the inflammation scores to be reduced to ~1.5 (*Figure 4E*).

Weight loss relates nonlinearly to lung injury and inflammation

To monitor disease progression, weight loss was measured daily throughout the course of infection (*Figure 5*). During the first 5 d pi, animals gradually lost ~4% of their initial weight. This was followed by a sharper drop (8%) at 6 d pi. Animal weights increased slightly at 7 d pi (~6%) before reaching peak weight loss (10–14%) at 8 d pi. Following virus resolution, the animals' weights began to restore as the inactive lesions resolved (9–10 d pi; *Figure 5A*). Weight loss was reduced during CD8$^+$ T cell depletion (*Figure 5A*). Plotting weight loss against the percent total (active and inactive) lesioned area of the lung shows the similarity in their dynamics (*Figure 5A*) and revealed a nonlinear relation (*Figure 5B*). To further quantify their relationship, we fit the saturating function $L(W) = l_{max}W^n/(W^n + K_w^n)$ to these data, where L is the percent total lesioned area, W is percent weight loss, l_{max} is the maximum rate of the interaction, K_w is the half-saturation constant, and n is the Hill coefficient. This function provided a close fit to the data ($R^2 = 0.92$; black line in *Figure 5B*)
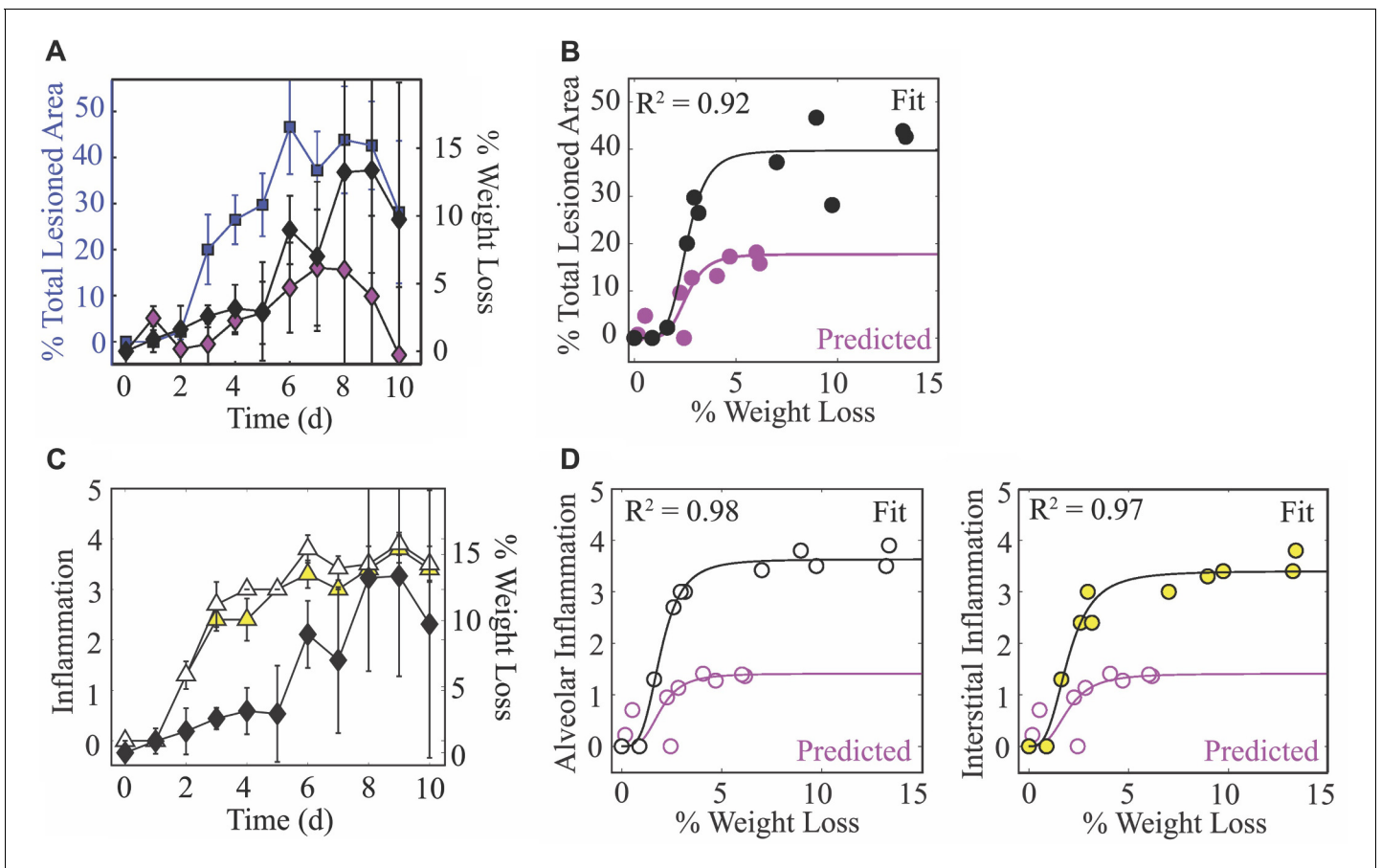
Figure 5. Weight loss dynamics and its relation to lung injury and inflammation. (**A**) The percent total (active and inactive) lesion (blue squares) plotted together with the percent weight loss (black diamonds) to illustrate their similar dynamics. (**B**) Fit of a saturating function ($L(W) = l_{max} W^n/(K_w^n + W^n)$; black line) to the mean percent total lesioned area (L) and mean weight loss (W) for all time points (black circles). The best-fit parameters were $l_{max} = 39.7\%$ total lesioned area, $K_w = 2.6\%$ weight loss, and $n = 5.2$. The magenta circles are the predicted percent total lesioned area (**Figure 4D**) with the corresponding weight loss during CD8 depletion, and the magenta line is the prediction using the best-fit parameters ($K_w = 2.6\%$ weight loss and $n = 5.2$) together with the maximum predicted percent total lesion ($l_{max} = 17.73\%$ total lesioned area). (**C**) The alveolar (white triangles) and interstitial (yellow triangles) inflammation plotted together with the percent weight loss (black diamonds). (**D**) Fit of a saturating function (black line) to the mean alveolar (white circles) and interstitial (yellow circles) inflammation scores and mean weight loss for all time points. The best-fit parameters for alveolar inflammation (white circles; black line) were $l_{a_{max}} = 3.63$ score, $K_{a_w} = 1.95\%$ weight loss, and $n_a = 3.65$, and for interstitial inflammation were $l_{i_{max}} = 3.40$ score, $K_{i_w} = 1.96\%$ weight loss, and $n_i = 3.15$. The magenta circles are the predicted percent inflammation score (**Figure 4E**) with the corresponding weight loss during CD8 depletion, and the magenta line is the prediction using the best-fit parameters ($K_{a_w} = 1.95\%$ weight loss, $n_a = 3.65$; $K_{i_w} = 1.96\%$ weight loss, $n_i = 3.15$) together with the maximum predicted inflammation ($l_{max} = 1.41$ score).

with best-fit parameters $l_{max} = 39.7\%$ total lesioned area, $K_w = 2.58\%$ weight loss, and $n = 5.24$. Plotting the estimated percent total lesion during CD8$^+$ T cell depletion (**Figure 4D**) together with the measured weight loss (**Figure 5A**) also supported the nonlinear relation. Using the same best-fit parameters ($K_w = 2.58\%$ weight loss and $n = 5.24$) together with the predicted maximum percent total lesion ($l_{max} = 17.73\%$ total lesioned area) showed the accuracy of this function (magenta line in **Figure 5D**). Weight loss was also nonlinearly correlated to the alveolar and interstitial inflammation scores (**Figure 5C**), although the relation was slightly different compared to that for the lung injury data. Fitting the same function to these data independently for alveolar and interstitial inflammation also provided a close fit ($R^2 = 0.98$ and $R^2 = 0.97$; black lines in **Figure 5D**). Best-fit parameters for alveolar inflammation were $l_{a_{max}} = 3.63$ score, $K_{a_w} = 1.95\%$ weight loss, and $n_a = 3.65$. Best-fit parameters for interstitial inflammation were $l_{i_{max}} = 3.40$ score, $K_{i_w} = 1.96\%$ weight loss, and $n_i = 3.15$. For the CD8-depleted case, plotting the estimated inflammation (**Figure 4E**) together with the measured weight loss (**Figure 5A**) again supported the nonlinear relation. In addition, using the same

best-fit parameters ($K_{a_w} = 1.95\%$ weight loss, $n_a = 3.65$; $K_{i_w} = 1.96\%$ weight loss, $n_i = 3.15$) together with the predicted maximum inflammation score ($l_{i_{max}} = 1.41$ score) showed the accuracy (magenta line in *Figure 5D*).

Discussion

Influenza A virus infections pose a significant threat to human health, and it is crucial to understand and have tools that can predict how the virus spreads within the lower respiratory tract, how specific immune responses contribute to infection control, and how these relate to disease progression. Although it has been difficult to directly relate these features and obtain high quality data from the lower respiratory tract in humans, we circumvented the challenge by pairing comprehensive experimental data with robust mathematical models and analyses. Our iterative model-driven experimental approach (*Smith, 2018a*; *Smith, 2018b*) revealed important dynamic relations between virus, infected cells, immune cells, lung damage, inflammation, and disease severity (summarized in *Figure 6*). Identifying these nonlinear connections allows for more accurate interpretations of viral
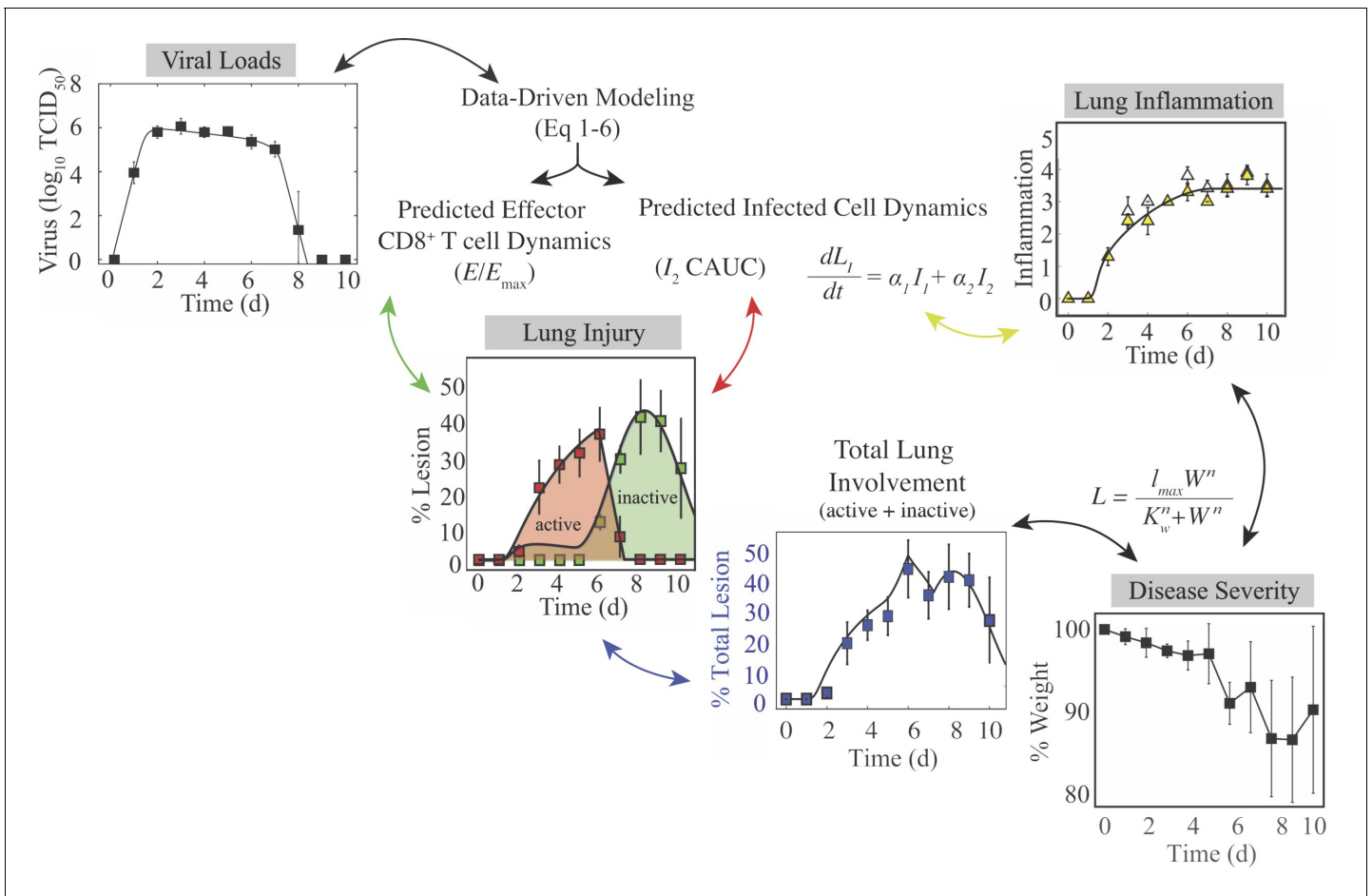

Figure 6. Summary of the connections between the kinetics of virus, infected cells, CD8+ T cells, lung injury, lung inflammation, and disease severity. Summary of the relations between the dynamics of virus, infected cells, CD8+ T cells, lung lesions, lung inflammation, and weight loss established by our analysis. Given that viral loads and weight loss are the most easily measured variables, our mathematical model (*Equation (1)-(6)*) could be used to estimate the kinetics of infected cells, CD8+ T cells, and inflammation. The cumulative area under the curve (CAUC) of the productively infected cell dynamics (I_2) yields an estimate of the percent lung infected (active lesion) while the predicted relative CD8$_E$ dynamics (E/E_{max}) yields an estimate of the percent lung resolved (inactive lesion). The total amount of lung involved (% lung infected and % lung resolved) or the inflammation scores can then be used to estimate weight loss through the functions $L_L(W)$ and $L_I(W)$. These connections could be reversed and weight loss used to estimate viral load kinetics.

infection data and significant improvement in our ability to predict disease severity, the likelihood of complications, and therapeutic efficacy.

Our histomorphometric data and analyses provided a robust quantification of the extent of influenza virus infection within the lung and the dynamics of lung injury and inflammation. The images look strikingly similar to CT scans and postmortem histopathology from infected patients, which also show extensive bilateral damage and cytopathic effects in epithelial cells (*Kohr et al., 2010*; *Li et al., 2011*; *Ajlan et al., 2009*; *Soto-Abraham et al., 2009*; *Gill et al., 2010*; *Li et al., 2012*; *Shieh et al., 2010*). In addition, our results agree with weekly CT imaging of hospitalized patients infected with the 2009 H1N1 influenza virus showing that the damage worsens during the first week of illness and that cell proliferation begins in the second week (*Li et al., 2012*). Further investigating the utility of CT imaging could enhance the translatability of our findings. The model's 95% CI predictions of the lesioned area nicely captured the heterogeneity in the data (*Figure 4*), which is remarkable given the minimal variability in the virus and CD8$^+$ T cell data and model fit (*Figure 1*). The differential heterogeneity suggests that small changes to lung viral loads can induce significant changes in disease severity. Indeed, this has been observed in both humans and animals when antivirals are administered (*Toniolo Neto, 2014*; *Baloxavir Marboxil Investigators Group et al., 2018*; *Treanor et al., 2000*; *Moscona, 2005*; *Gubareva et al., 2000*; *Koshimichi et al., 2018*) or when host responses are experimentally modulated (*Channappanavar et al., 2016*; *Szretter et al., 2009*; *Iwasaki and Nozima, 1977*). It was also observed in our CD8 depletion data, where our model predicted a significant reduction in the lesioned area (*Figure 4*) while viral loads were only slightly lower (*Figure 3*). This may indicate that viral loads are generally not a reliable measure of infection severity, and the knowledge should aid future studies seeking to estimate therapeutic efficacy or the effects of immune modulation. There was a slight over-estimation of the inactive lesion early in the infection (1–5 d pi, dark gray shading; *Figure 4*) when using the fit to the total CD8$^+$ T cells, which was abrogated when using the CD25$^-$CD43$^+$CD8$^+$ T cells. However, these cells underestimated the total lesion at 6–7 d pi, suggesting contributions from other CD8$^+$ phenotypes. In general, modeling different CD8$^+$ T cell phenotypes may help clarify their *in vivo* functions and better define the rates of CD8-mediated infected cell clearance. Although our results suggest that this is not necessarily required, they may be more critical to consider when predicting the response of preexisting and potentially cross-reactive immunity particularly given that memory resident T cells are only beginning to be understood (*Zens et al., 2016*; *Slütter et al., 2017*; *Van Braeckel-Budimir et al., 2018*; *Wakim et al., 2015*; *Uddbäck et al., 2021*).

The new knowledge about the extent of infection within the lung also uncovered the nonlinear connection between disease severity and various measures of lung pathology (*Figure 5*). This discovery is significant because it suggests there is a unique link to the extent of both lung injury and inflammation, which are often used interchangeably yet have distinct dynamics (*Figure 4*) and correlate to different immune responses (*Figure 4—figure supplements 1–2*). In the same vein, both measurements can be estimated using the dynamics of infected cells (*Figure 4*) but with independent mathematical relations (CAUC of I_2 versus *Equation (7)*). Our CD8 depletion data (*Figure 3*) and other experimental studies using histomorphometry (*Marathe et al., 2016*) corroborate a relationship between weight loss and lung pathology during IAV infection. For example, animals treated with antivirals in various conditions (single or combination therapy and in immunocompetent or immunosuppressed hosts) demonstrated that, although viral loads are not always significantly reduced, the antiviral-induced reductions in weight loss were paired with decreased infected areas of the lung (*Marathe et al., 2016*). Further examining lung injury and inflammation kinetics and their connection to weight loss in various experimental infection settings (e.g., different ages or sex, under therapy, other strains or viruses, etc.) and deciphering how innate and humoral responses contribute to these measurements should improve our predictive capabilities. In addition, the nonlinearity of the connections warrants further investigation as it could indicate cooperativity of multiple mechanisms. Studies such as these may be particularly helpful in understanding the exacerbated morbidity and mortality in elderly individuals, where there are lower viral loads, increased weight loss, symptoms, and/or mortality within animal models (*Toapanta and Ross, 2009*; *Smith et al., 2019*). Because murine models are imperfect systems with important immunologic and physiologic distinctions from humans (*Mestas and Hughes, 2004*), uncovering how our results translate to human infection with novel or circulating influenza viruses and identifying the corresponding, tractable human symptom that could be a robust predictor of disease would be ideal. However, this could

be arduous due to inherent human and viral heterogeneity and contributions from co-morbidities and complex immunologic histories.

Despite their limitations, animal models are used to make viral and immunological discoveries and to develop and test therapeutics and vaccines (reviewed in *Thangavel and Bouvier, 2014*; *Margine and Krammer, 2014*; *Smith and McCullers, 2014*), and this work demonstrates a significant potential for the easily obtained weight loss data to be used, analyzed, and interpreted within both modeling and experimental studies. In our data and others' animal data, there is a spike in weight loss, symptom score, and/or inflammation at ~6 d pi (*Music et al., 2014*; *Kugel et al., 2009*; *Lu et al., 2018*; *Huang et al., 2017*; *Figure 5*). Our data suggests that this may be due to $CD8_E$ activity while the infection continues to spread. The increase in animal weights starting at 7 d pi is concurrent with the decline in infected lesions (*Figure 5*). Interestingly, there was no corresponding decrease in inflammation, and the spike was not apparent in the CD8 depletion data where severity was reduced. The subsequent increase in weight loss following infection resolution (8–9 d pi; *Figure 4C*) could be attributed to $CD8^+$ T cell-mediated pathology and/or to ongoing inflammation. The tighter correlation to inflammation might suggest the latter; however, some human and animal studies indicate that large numbers of $CD8^+$ T cells pose a risk of acute lung tissue injury (*Duan and Thomas, 2016*; *Moskophidis and Kioussis, 1998*; *Mauad et al., 2010*; *Rygiel et al., 2009*; *La Gruta et al., 2007*). According to our model predictions, excessive $CD8^+$ T cell numbers may augment disease progression yet do not improve recovery time (*Appendix 3—figure 2*). Instead, an earlier onset of $CD8_E$ proliferation (i.e., smaller τ_E) would be required to significantly shorten the infection (*Appendix 3—figure 2*). This aligns with evidence that hosts with adaptive immune responses primed by vaccine or prior infection recover more rapidly (*Duan et al., 2015*; *Weinfurter et al., 2011*). While higher $CD8^+$ T cell numbers have little impact on viral kinetics, our model and data agree with clinical and experimental studies from a wide range of host species that impaired $CD8^+$ T cell responses can prolong an IAV infection (*Wang et al., 2015*; *Miao et al., 2010*; *McMichael et al., 1983*; *Yap and Ada, 1978*; *Wells et al., 1981*; *Bender et al., 1992*). In some scenarios, such as in immunocompromised hosts, virus can persist for up to several weeks if $CD8^+$ T cell-mediated clearance is unsuccessful (*Figure 3*; *Wang et al., 2015*; *Eichelberger et al., 1991*; *Hou et al., 1992*; *Xue et al., 2017*; *Memoli et al., 2014*). The bifurcation in recovery time revealed by the model suggests that this may occur when the number of lung-specific $CD8^+$ T cells are less than 2.31×10^5 cells (*Figure 3D–E*). Our CD8 depletion data show that the precise number will be dependent on other infection variables. Minimally, we would expect this number to vary depending on parameters like the dose, rate of virus replication, degree of prior immunity, and/or the infected cell number and lifespan, which has been noted in another modeling study that detailed similar bifurcating behavior (*Yates et al., 2011*). Although some previously published models also suggested delayed resolution with depleted $CD8^+$ T cell responses (*Dobrovolny et al., 2013*; *Miao et al., 2010*; *Cao et al., 2016*; *Lee et al., 2009*), this bifurcation has not been observed and their estimated delays in recovery do not amount to the long-lasting infections in immunodeficient patients (*Wang et al., 2015*; *Eichelberger et al., 1991*; *Hou et al., 1992*). Our model's ability to capture the dynamics when $CD8^+$ T cells are depleted is encouraging, and the data are an important reminder that experimental modulation of cell populations (e.g., through depletion or genetic knockouts) is complicated and that the data from such systems should be interpreted cautiously. It also brings into question studies that have used these types of data without validated mathematical models or quantification of other immunological variables.

Our data and analyses provided strong support that the infected cell density impacts the rate at which they are cleared by effector $CD8^+$ T cells ($CD8_E$) (*Figures 3–4*, *Figure 4—figure supplement 1*). Although $CD8^+$ T cell dynamics can be somewhat replicated when assuming the density dependence lies within their expansion, that assumption could not recover the viral load dynamics (*Appendix 1—figure 1*). Discriminating between these mechanisms is difficult *in vivo*, but the ability of the model in *Equation (1)-(6)* to capture the entire time course of $CD8_E$ dynamics in multiple scenarios is compelling. Regardless of the mechanism, we first detected this density-dependence in a model that excluded specific immune responses (see Appendix 2) (*Smith et al., 2018*). Simple models like that one are useful to capture nonlinearities, but they cannot distinguish between different mechanisms.

Several factors may contribute to the density-dependent change in the rate of $CD8_E$-mediated clearance. One possibility is that the slowed rate of clearance at high infected cell densities is due to

a 'handling time' effect, which represents the time required for an immune cell to remove an infected cell (e.g., as in *Smith et al., 2018*; *Li and Handel, 2014*; *Le et al., 2014*; *Graw and Regoes, 2009*; *Gadhamsetty et al., 2014*; *Pilyugin and Antia, 2000*; *Smith et al., 2011b*). When $CD8_E$ interact with infected cells, a complex is formed for ~20–40 min (*Mempel et al., 2006*; *Deguine et al., 2010*; *Zagury et al., 1975*; *Yannelli et al., 1986*; *Perelson and Bell, 1982*). Because $CD8_E$ could not interact with other infected cells during this time, the global rate of infected cell clearance would be lowest when infected cells outnumber $CD8_E$. In addition, contact by a single $CD8_E$ may be insufficient to remove an infected cell (*Halle et al., 2016*). Infected cell clearance is more frequently observed after interactions with multiple $CD8_E$, with an average of 3.9 contact events either serially or simultaneously (*Halle et al., 2016*). Thus, the high density of infected cells early in the infection reduces the probability that a single virus-infected cell would be targeted a sufficient number of times to induce cell death. However, as $CD8_E$ accumulate and the density of infected cells decreases (*Figure 3A*), the probability of simultaneous interactions will increase. These interactions may also be influenced by $CD8_E$ movement, where their velocity slows at the height of infected cell clearance (6–8 d pi) (*Lambert Emo et al., 2016*; *Matheu et al., 2013*). This should reduce the time required to remove an infected cell and, thus, result in a higher efficiency. Moreover, it is possible that spatial limitations also contribute, such that a high infected cell density may hinder $CD8^+$ T cells from reaching infected cells on the interior of the infected tissue. Crowding of immune cells at the periphery of infected lesions has been observed in other infections (e.g., in tuberculosis granulomas [*Ulrichs et al., 2004*; *Russell et al., 2009*]) and has been suggested in agent-based models of influenza virus infection (*Levin et al., 2016*).

In addition to illuminating the connections between viral kinetics and pathology, the histomorphometric data validated the model's infected cell dynamics (*Figure 4B*). The dynamics of susceptible and infected cells throughout the infection and the accuracy of the target cell limited approximation used within influenza viral kinetic models have been questioned for several years (*Smith and Perelson, 2011*; *Smith, 2018b*; *Beauchemin and Handel, 2011*; *Ahmed et al., 2017*; *Gallagher et al., 2018*; *Boianelli et al., 2015*; *Handel et al., 2018*). The ability of the model to accurately predict the histomorphometry and $CD8^+$ T cell depletion data corroborates the use of this approximation, which assumes a limited number of available target cells and describes their decline by infection only. Although the slowing of viral loads beginning at 2 d pi could be due to a variety of innate immune-mediated mechanisms (e.g., macrophages, neutrophils, type I interferons, etc.), adding more complex dynamics to our model was unnecessary to describe the data. Further, the model and data agree that there are few infected cells during the time when viral loads are growing most rapidly (0–2 d pi; *Figures 1B* and *4B*). We previously used this information to derive approximations for the model and gain deeper insight into how each parameter influences the kinetics (*Smith et al., 2010*), which has helped numerous studies interpret their results (*Miao et al., 2010*; *Smith et al., 2011a*; *Smith, 2018b*; *Holder and Beauchemin, 2011*). The data also supports the model's hypothesis that that there is minimal clearance of infected cells prior to $CD8_E$ expansion (*Figure 4*). The knowledge of the model's accuracy and of the spatiality in the lung should aid investigation into the mechanisms that limit virus growth during the early stages of the infection.

Employing targeted model-driven experimental designs to examine and validate theoretical predictions like the ones presented here is pivotal to elucidating the mechanisms of infection spread and clearance (*Smith, 2018b*). Examining other infections (e.g., coronaviruses), modifications to the dynamics (e.g., lethal doses), and the connection between lung measurements and those more easily acquired from upper respiratory tract will help refine the dynamical links between virus, host immune responses, and disease severity and identify their generalizability. Determining the factors that influence disease severity is vital to understanding the disproportionate mortality in at-risk populations (e.g., elderly) and to improving therapeutic design. This is particularly important because current antivirals alleviate symptoms but do not always effectively lower viral loads (*Toniolo Neto, 2014*; *Baloxavir Marboxil Investigators Group et al., 2018*; *Treanor et al., 2000*; *Moscona, 2005*; *Gubareva et al., 2000*; *Koshimichi et al., 2018*). The predictive capabilities of validated models like the one here should prove useful in forecasting infection dynamics for a variety of scenarios. These tools and analyses provide a more meaningful interpretation of infection data, new ways to interpret weight loss data in animal models, and a deeper understanding of the progression and resolution of the disease, which will undoubtedly aid our ability to effectively combat influenza.

Materials and methods

Ethics statement

All experimental procedures were performed under protocols O2A-020 or 17–096 approved by the Animal Care and Use Committees at St. Jude Children's Research Hospital (SJCRH) or the University of Tennessee Health Science Center (UTHSC), respectively, under relevant institutional and American Veterinary Medical Association (AVMA) guidelines. All experimental procedures were performed in a biosafety level two facility that is accredited by the American Association for Laboratory Animal Science (AALAS).

Mice

Adult (6-week-old) female BALB/cJ mice were obtained from Jackson Laboratories (Bar Harbor, ME) or Charles River Laboratories (Wilmington, Massachusetts). Mice were housed in groups of five mice in high-temperature 31.2 cm × 23.5 cm × 15.2 cm polycarbonate cages with isolator lids (SJCRH) or in 38.2 cm × 19.4 cm × 13.0 cm solid-bottom polysulfone individually ventilated cages (UTHSC). Rooms used for housing mice were maintained on a 12:12 hr light:dark cycle at 22 ± 2°C with 50% humidity in the biosafety level two facility at SJCRH (Memphis, TN) or UTHSC (Memphis, TN). Prior to inclusion in the experiments, mice were allowed at least 7 days to acclimate to the animal facility such that they were 7 weeks old at the time of infection. Laboratory Autoclavable Rodent Diet (PMI Nutrition International, St. Louis, MO; SJCRH) or Teklad LM-485 Mouse/Rat Sterilizable Diet (Envigo, Indianapolis, IN; UTHSC) and autoclaved water were available *ad libitum*. All experiments were performed under an approved protocol and in accordance with the guidelines set forth by the Animal Care and Use Committee at SJCRH or UTHSC.

Infectious agents

All experiments were done using the mouse adapted influenza A/Puerto Rico/8/34 (H1N1) (PR8).

Infection experiments

The viral infectious dose (TCID$_{50}$) was determined by interpolation using the method of *Reed and Muench, 1938* using serial dilutions of virus on Madin-Darby canine kidney (MDCK) cells. Mice were intranasally inoculated with 75 TCID$_{50}$ PR8 diluted in 100 µl of sterile PBS. In a subset of animals, CD8$^+$ T cells were depleted by IP injection at days −2, 0, 3, and 7 pi with 100 µg of the rat anti-CD8α antibody (clone 2.43) that was purified from ATCC hybridoma (per manufacturer instructions) in 250 µl of PBS. Depletion efficiency was confirmed in the lung and spleen as described below. Mice were weighed at the onset of infection and each subsequent day to monitor illness and mortality. Mice were euthanized if they became moribund or lost 30% of their starting body weight. For viral load and total CD8$^+$ T cell quantification, experiments were repeated three times and in each facility to ensure reproducibility and two complete experiments (ten animals per time point) were used for these studies. For all other experiments, the data was compared to prior results in addition to being repeated at select time points to ensure reproducibility, and one complete experiment (five animals per time point) was used. For pathology scoring and histomorphometry quantitation, five animals per time point were used. Power was calculated using G*Power.

Lung harvesting for viral and cellular dynamics

For total CD8$^+$ T cell quantification, mice were euthanized by CO$_2$ asphyxiation. To distinguish blood-borne CD8$^+$ T cells from those in the lung parenchyma, deeply anesthetized mice (5% isoflurane) were retro-orbitally injected with 3 µg of anti-CD45 antibody (PerCP, clone 30-F11, Biolegend) 3 min prior to euthanasia (*Anderson et al., 2012*; *Keating et al., 2018*). Mice were then euthanized by 33% isoflurane inhalation and their lungs perfused with 10 ml PBS prior to removal. For all experiments, lungs were then aseptically harvested, washed three times in PBS, and placed in 500 µl sterile PBS. Whole lungs were digested with collagenase (1 mg/ml, Sigma C0130), and physically homogenized by syringe plunger against a 40 µm cell strainer. Cell suspensions were centrifuged at 4°C, 500xg for 7 min. The supernatants were used to determine the viral titers (TCID$_{50}$) by serial dilutions on MDCK monolayers. Following red blood cell lysis, cells were washed in MACS buffer (PBS, 0.1M EDTA, 0.01M HEPES, 5 mM EDTA and 5% heat-inactivated FBS). Cells were then counted with

trypan blue exclusion using a Cell Countess System (Invitrogen, Grand Island, NY) and prepared for flow cytometric analysis as indicated below.

Lung titers

For each animal, viral titers were obtained using serial dilutions on MDCK monolayers and normalized to the total volume of lung homogenate supernatant. The resulting viral loads are shown in *Figure 1B*, provided in *Source data 1*, and were previously published and utilized for calibration of the density-dependent model (see Appendix 2; *Smith et al., 2018*).

Flow cytometric analysis

Flow cytometry (LSRII, BD Biosciences, San Jose, CA (SJCRH) or ZE5 Cell Analyzer, Bio-Rad, Hercules, CA (UTHSC)) was performed on the cell pellets after incubation with 200 µl of a 1:2 dilution of Fc block (human-γ globulin) on ice for 30 min, followed by viability (Biolegend, Zombie Violet Fixable Viability Kit) and surface marker staining with anti-mouse antibodies. For total $CD8^+$ T cell, macrophage, and neutrophil quantification, we used antibodies CD3e (BV786, clone 145–2 C11, Biolegend), CD4 (PE-Cy5, clone RM4-5, BD Biosciences), CD8α (BV605, clone 53–6.7, BD Biosciences), Ly6C (APC, clone HK1.4, eBioscience), F4/80 (PE, clone BM8, eBioscience), CD11c (eFluor450, clone N418, eBioscience), CD11b (Alexa700, clone M1/70, BD Biosciences), MHC-II (FITC, clone M5/114.15.2, Invitrogen), CD49b (APCe780, clone DX5, eBioscience), and Ly6G (PerCp-Cy5.5, clone 1A8, Biolegend). The data were analyzed using FlowJo 10.4.2 (Tree Star, Ashland, OR) where viable cells were gated from a forward scatter/side scatter plot and singlet inclusion. Following neutrophil ($Ly6G^{hi}$) and subsequent macrophage ($CD11c^{hi}F4/80^{hi}$) exclusion, $CD8^+$ T cells were gated as $CD3e^+DX5^-CD4^-CD8^+$.

To distinguish blood borne $CD8^+$ T cells from those in the lung parenchyma, we used antibodies CD3e (BV786, clone 145–2 C11, Biolegend), CD4 (FITC, clone RM4-5, Biolegend), CD8α (BV605, clone 53–6.7, BD Biosciences), B220 (APCe780, clone RA3-6B2, eBioscience), CD49b (APCe780, clone DX5, eBioscience), CD62L (PE-Cy7, clone MEL-14, Biolegend), CD69 (PE, clone H1.2F3, Biolegend), CD44 (PE-Dazzle594, clone IM7, Biolegend), CD25 (Alexa700, clone PC61, Biolegend), CD43 (APC, clone 1B11, Biolegend), CD127 (PE-Cy5, clone A7R34, Biolegend), and CD103 (BV711, clone 2E7, Biolegend) or CD314 (NKG2D) (BV711, clone CX5, BD Bioscience). The data were analyzed using FlowJo 10.6.2 (Tree Star, Ashland, OR) where viable cells were gated from a forward scatter/side scatter plot, singlet inclusion, and viability dye exclusion. Blood borne $CD8^+$ T cells were gated as $CD45^+$ and those in the lung parenchyma as $CD45^-$. The total in each sub-population was gated as $CD3e^+B220^-DX5^-CD4^-CD8^+$. IAV-specific $CD8^+$ T cells were then gated as $CD25^+CD43^+$ (recently activated), $CD25^-CD43^+$ (effector) (*Keating et al., 2018*), and $CD43^-CD127^+CD103^+CD69^+$ (long-lived memory). Expression of CD44, CD69, CD62L, and NKG2D were also assessed to ensure appropriate classification.

For all experiments, the absolute numbers of $CD8^+$ T cells were calculated based on viable events analyzed by flow cytometry as related to the total number of viable cells per sample. The data are provided in *Source data 1*. We use the kinetics of the total number of $CD8^+$ T cells (non-perfused lung; 'total'), the total number of $CD8^+$ T cells in the lung parenchyma (perfused lung; 'lung-specific'), and virus-specific $CD8^+$ T cell phenotypes in the lung parenchyma as defined by surface staining (described above). We chose this approach because the use of tetramers yields epitope-specific cell dynamics that vary in time and magnitude (e.g., as in *Toapanta and Ross, 2009*; *Keating et al., 2018*) and would complicate the model and potentially skew the results. In addition, tetramer staining is not available for all epitopes in BALB/cJ mice and they may underestimate the dynamics of IAV-specific cells (*Keating et al., 2018*). The gating strategies are shown in *Figure 1—figure supplement 2*.

Lung immunohistopathologic and immunohistochemical (IHC) evaluation

The lungs from IAV-infected mice were fixed via intratracheal infusion and then immersion in 10% buffered formalin solution. Tissues were paraffin embedded, sectioned, and stained for influenza virus using a primary goat polyclonal antibody (US Biological, Swampscott, MA) against influenza A, USSR (H1N1) at 1:1000 and a secondary biotinylated donkey anti-goat antibody (sc-2042; Santa Cruz Biotechnology, Santa Cruz, CA) at 1:200 on tissue sections subjected to antigen retrieval for 30 min

at 98°C. The extent of virus spread was quantified by capturing digital images of whole-lung sections (two dimensional) stained for viral antigen using an Aperio ScanScope XT Slide Scanner (Aperio Technologies, Vista, CA) then manually outlining defined fields. Alveolar areas containing virus antigen-positive pneumocytes were highlighted in red (defined as 'active' infection), whereas lesioned areas containing minimal or no virus antigen-positive debris were highlighted in green (defined as 'inactive' infection). Lesions containing a mix of virus antigen-positive and antigen-negative pneumocytes were highlighted in orange (defined as 'mixed' infection). The percentage of each defined lung field was calculated using the Aperio ImageScope software. Pulmonary lesions in HE-stained histologic sections were assigned scores based on their severity and extent. Representative images from each group and quantitative analyses (five animals/group) of viral spread and lung pathology during IAV infection are shown in *Figure 4*, and provided in *Source data 1*.

CD8$^+$ T cell model

To examine the contribution of CD8$^+$ T cells to the biphasic viral load decay, we expanded the density-dependent (DD) model (see Appendix 2) to include two mechanisms of infected cell clearance (non-specific clearance (δ) and CD8$^+$ T cell-mediated clearance ($\delta_E(I_2, E)$)) and two CD8$^+$ T cell populations: effector (E, denoted CD8$_E$) and memory (E_M, denoted CD8$_M$) CD8$^+$ T cells. The model is given by *Equation (1)-(6)*.

$$\frac{dT}{dt} = -\beta TV \tag{1}$$

$$\frac{dI_1}{dt} = \beta TV - kI_1 \tag{2}$$

$$\frac{dI_2}{dt} = kI_1 - \delta I_2 - \delta_E(I_2, E)I_2 \tag{3}$$

$$\frac{dV}{dt} = pI_2 - cV \tag{4}$$

$$\frac{dE}{dt} = \xi(E)I_2 + \eta EI_2(t - \tau_E) - d_E E \tag{5}$$

$$\frac{dE_M}{dt} = \zeta E(t - \tau_M) \tag{6}$$

In this model, target cells become infected with virus at rate βV per day. Once infected, cells enter an eclipse phase (I_1) before transitioning at rate k per day to a productively-infected state (I_2). These infected cells produce virus at rate p TCID$_{50}$ per infected cell per day, and virus is cleared at rate c per day. Virus-producing infected cells (I_2) are cleared by non-specific mechanisms (e.g., apoptosis and/or innate immune responses) at a constant rate δ per day. Innate immune responses were excluded from the model because the viral load data is linear during the time where they act (2–7 d pi) and, thus, additional equations cannot improve the fit. Productively infected cells are cleared by CD8$_E$ at rate $\delta_E(I_2, E) = \delta_E E/(K_{\delta_E} + I_2)$ per day, where the rate of infected cell clearance is δ_E/K_{δ_E} per CD8$_E$ per day and K_{δ_E} is the half-saturation constant. The CD8$_E$-mediated clearance rate ($\delta_E(I_2, E)$) is dependent on the density of infected cells and is similar to the infected cell clearance term in the DD model (see *Equation (A11)*; *Smith et al., 2018*). Similar density-dependent forms have also been used in models that describe the CD8$^+$ T cell response to other virus infections (*De Boer and Perelson, 1998*; *Li and Handel, 2014*; *Gadhamsetty et al., 2014*). Models that exclude this density-dependence were examined, but these models resulted in a statistically poor fit to the data as defined by the Akaike Information Criteria (AIC) (*Supplementary file 2*). This is due in part to the increase of CD8$^+$ T cells from 3-5 d pi (*Figure 1*). We did examine a model that excluded these dynamics and included CD8$^+$ T cell expansion as a density-dependent function (e.g., $\eta EI_2(t - \tau_E)/(K_I + I_2)$) while keeping a linear rate of CD8-mediated infected cell clearance ($\delta_E EI_2$) (see Appendix 1). This model was adapted from other published models (*Conway and Perelson,*

2015; *Bonhoeffer et al., 2000*; *Baral et al., 2019*) and can produce similar dynamics from 6-10 d pi, but it was not statistically supported by our data (*Supplementary file 1*). We further tested the model in *Baral et al., 2019*, but this model could not fit our data and lacked statistical support (*Supplementary file 1*).

The model assumes that the initial CD8$_E$ influx in the lung is proportional to infected cells at rate $\xi(E) = \xi/(K_E + E)$ CD8$_E$ per cell per day, which is down-regulated by the CD8$_E$ already present in the lung. The associated half-saturation constant is K_E. Similar terms for CD8$_E$ regulation have been used in modeling HIV infections (*De Boer and Perelson, 1998*; *Müller et al., 2001*) and in models that examined CD8$^+$ T cell proliferation mechanisms (*De Boer and Perelson, 1995*). We also examined whether their influx is proportional to infected cells at a delay (i.e., $\xi(E)I(t - \tau_I)$). While this modification better captured the initial increase in CD8$^+$ T cells, the additional parameter was not supported. In our model, CD8$_E$ expansion occurs at rate η per infected cell per day with time delay τ_E. This term accounts for local CD8$_E$ proliferation in the lung (*McGill and Legge, 2009*; *Lawrence et al., 2005*) and migration of CD8$_E$ from secondary lymphoid organs (*Zhang and Bevan, 2011*; *Bedoui and Gebhardt, 2011*; *Wu et al., 2011*; *Kang et al., 2011*). The delay may signify the time it takes CD8$_E$ to become activated by antigen presenting cells, differentiate, proliferate, and/or migrate to the infection site. The lung CD8$_E$ population declines due to cell death and/or emigration at rate d_E per day. These cells transition to CD8$_M$ (E_M) at rate ζ CD8$_M$ per CD8$_E$ per day after τ_M days. The model schematic and fit to the viral load, total, effector, and memory CD8$^+$ T cell data are in *Figure 1*. All code is provided in *Source code 1*.

Inflammation model

To estimate the alveolar and interstitial inflammation without modeling other cell classes (e.g., macrophages and neutrophils), we assumed that inflammation in the lung (L_I) was proportional to the infected cells (I_1 and I_2) according to the equation,

$$\frac{dL_I}{dt} = \alpha_1 I_1 + \alpha_2 I_2, \tag{7}$$

where $\alpha_{1,2}$ has units of score/cell/d and defines the inflammation score contribution from each infected cell class. A decay term was excluded because inflammation does not resolve on the timescale of our data.

Parameter estimation

Given a parameter set θ, the cost $C(\theta)$ was minimized across parameter ranges using an Adaptive Simulated Annealing (ASA) global optimization algorithm (*Smith et al., 2018*) to compare experimental and predicted values of virus (V; $\log_{10}$ TCID$_{50}$/lung) and $\log_{10}$ total CD8$^+$ T cells/lung ($\hat{E} = E + E_M + \hat{E}_0$, where $\hat{E}_0$ is the initial number of CD8$^+$ T cells at 0 d pi), or $\log_{10}$ TCID$_{50}$/lung virus (V), $\log_{10}$ effector CD8$^+$ T cells/lung ($\hat{E} = E + \hat{E}_0$), and $\log_{10}$ memory CD8$^+$ T cells/lung ($\hat{E}_M = E_M + \hat{E}_{M_0}$). The cost function is defined by,

$$C(\theta) = \sum_{i,j}(V(\theta,t_i) - v_{i,j})^2 + \sum_{i,j}(\hat{E}_M(\theta,t_i) - m_{i,j})^2 + s_E\left[\sum_{i,j}(\hat{E}(\theta,t_i) - e_{i,j})^2 + \right.$$
$$\left. \sum_i \sqrt{\gamma_i}\left(\frac{\hat{E}(\theta,t_{i+1}) - \hat{E}(\theta,t_{i-1})}{t_{i+1} - t_{i-1}} - \frac{1}{\gamma_i}\sum_j \frac{e_{i+1,j} - e_{i-1,j}}{t_{i+1} - t_{i-1}}\right)^2\right],$$

where $(t_i, v_{i,j})$ is the viral load data, $(t_i, e_{i,j})$ is the total or effector CD8$^+$ T cell data, $(t_i, m_{i,j})$ is the memory CD8$^+$ T cell data, and $V(\theta,t_i)$, $\hat{E}(\theta,t_i)$, and $\hat{E_M}(\theta,t_i)$ are the corresponding model predictions. Here, $s_E = (v_{\max} - v_{\min})/(e_{\max} - e_{\min})$ is a scaling factor, and $\gamma_i = J_{i+1}J_{i-1}$ where J_i is the number of observations at time t_i. Errors of the $\log_{10}$ data were assumed to be normally distributed. To explore and visualize the regions of parameters consistent with the model, we fit *Equation (1)-(6)* to 2000 bootstrap replicates of the data. If the fit was within $\chi^2 = 0.05$ of the best-fit and the CD8 derivative was not a statistical outlier as determined by the function *isoutlier*, then the bootstrap was considered successful (*Smith et al., 2011a*; *Smith et al., 2013*; *Smith et al., 2018*). For each best-fit estimate, we provide 95% confidence intervals (CI) obtained from the bootstrap replicates (*Table 1*).

Calculations were performed either in MATLAB using a custom built ASA algorithm (*Smith et al., 2018*) or in Python using the *simanneal* package (*Perry, 2018*) followed by a L-BFGS-B (*Byrd et al., 1995*; *Zhu et al., 1997*) deterministic minimization through SciPy's *minimize* function. MATLAB *ode15s* and *dde23* or SciPy integrate.ode using *lsoda* and PyDDE (*Cairns, 2008*) were used as the ODE and DDE solvers.

Estimated parameters in the CD8$^+$ T cell model included the rates of virus infection (β), virus production (p), virus clearance (c), eclipse phase transition (k), non-specific infected cell clearance (δ), CD8$_E$-mediated infected cell clearance (δ_E), half-saturation constants (K_{δ_E} and K_E), CD8$_E$ infiltration (ξ), CD8$_E$ expansion (η), delay in CD8$_E$ expansion (τ_E), CD8$_E$ clearance (d_E), CD8$_M$ generation (ζ), delay in CD8$_M$ generation (τ_M), and the baseline number of CD8$^+$ T cells ($\hat{E}_0, \hat{M}_0$). Bounds were placed on the parameters to constrain them to physically realistic values. Because biological estimates are not available for all parameters, ranges were set reasonably large based on preliminary results and previous estimates (*Smith et al., 2018*). The rate of infection (β) was allowed to vary between $10^{-6} - 10^{-1}$ TCID$_{50}^{-1}$ d^{-1}, and the rate of virus production (p) between $10^{-1} - 10^3$ TCID$_{50}$ cell^{-1} d^{-1}. Bounds for the virus clearance rate (c) were 1 d^{-1} ($t_{1/2} = 16.7$ h) and 10^3 d^{-1} ($t_{1/2} = 1$ min). To ensure biological feasibility, the lower and upper bounds for the eclipse phase transition rate (k) were 4-6 d^{-1} as done previously (*Smith et al., 2018*).

The rate of non-specific infected cell clearance (δ) was given limits of 0.05–1 d^{-1}. The CD8$_E$-mediated infected cell clearance rate (δ_E) varied between $0.01 - 2$ cells CD8$_E^{-1}$ d^{-1}, and the associated half-saturation constant (K_{δ_E}) was bounded between 10^1–10^6 cells. The upper bound of δ_E was chosen to maintain the convergence of δ to nonzero values and consistency with prior results where δ approximates the slope of the first decay phase (*Smith et al., 2010*). Bounds for the rate of CD8$_E$ infiltration (ξ) were $10^2 - 10^6$ CD8$_E^2$ cell^{-1} d^{-1}, and bounds for the half-saturation constant (K_E) were 10^3-10^7 CD8$_E$. The CD8$_E$ expansion rate (η) varied between 10^{-8}–10^{-6} cell^{-1} d^{-1}, and the delay in CD8$_E$ expansion (τ_E) between 2–6 d. The rate of CD8$_E$ clearance (d_E) had limits of 0.05–2 d^{-1}. The rate of CD8$_M$ generation (ζ) varied between $0.01 - 1$ CD8$_M$ CD8$_E^{-1}$ d^{-1}, and the delay in CD8$_M$ generation (τ_M) varied between 3–4 d (total CD8$^+$ T cell fit) or 2–6 d pi (effector and memory CD8$^+$ T cell fit). Larger bounds were examined for this parameter; however, the parameter was non-identifiable in the total CD8$^+$ T cell fit and a small range was required for convergence. Bounds for the baseline number of CD8$^+$ T cells ($\hat{E}_0, \hat{E}_{M_0}$) were set to the upper and lower values of the data at 0 d pi ($3.0 \times 10^5 - 5.3 \times 10^5$ CD8 (total), $2.5 \times 10^2 - 1.4 \times 10^3$ CD8$_E$ (effector), $3.4 \times 10^2 - 8.0 \times 10^2$ CD8$_M$ (memory)).

The initial number of target cells ($T(0)$) was set to 10^7 cells (*Smith et al., 2011a*). The initial number of infected cells $I_1(0)$ was set to 75 cells to reflect an initial dose of 75 TCID$_{50}$ (*Smith et al., 2018*). We previously found that estimating $I_1(0)$, fixing $V(0) = 75$ TCID$_{50}$, or estimating $V(0)$ did not improve the fit and could not be statistically justified (*Smith et al., 2018*). The initial number of productively infected cells ($I_2(0)$), the initial free virus ($V(0)$), and the initial number of CD8$_E$ ($E(0)$) and CD8$_M$ ($E_M(0)$) were set to 0. All other parameter estimations were done as described in the text.

Linear regression

The function *polyfit* in MATLAB was used to perform linear regression on the percent active lesioned area, the percent inactive lesioned area, and the CD8$^+$ T cells during the expansion phase (5–8 d pi) and the contraction phase (9–10 d pi). Linear fits are shown in *Figure 4—figure supplement 1*.

Cumulative area under the curve

The function *cumtrapz* in MATLAB was used to estimate the cumulative area under the curve (CAUC) of the infected cells (I_2) for the best-fit model solution.

Acknowledgements

Additional information

Funding

Funder	Grant reference number	Author
National Institute of Allergy and Infectious Diseases	AI139088	Margaret A Myers Amanda P Smith Lindey C Lane Rosemary Aogo
National Institute of Allergy and Infectious Diseases	AI125324	Margaret A Myers Amanda P Smith Lindey C Lane David J Moquin Amber M Smith
National Institute of Allergy and Infectious Diseases	AI100946	Amber M Smith
American Lebanese Syrian Associated Charities	Internal Funding	Margaret A Myers Amanda P Smith Lindey C Lane David J Moquin Stacie Woolard Paul Thomas Peter Vogel Amber M Smith

Author contributions

Margaret A Myers, Software, Formal analysis, Investigation, Visualization, Writing - original draft; Amanda P Smith, Data curation, Formal analysis, Validation, Investigation, Visualization, Methodology, Writing - original draft, Writing - review and editing; Lindey C Lane, David J Moquin, Data curation; Rosemary Aogo, Formal analysis, Writing - review and editing; Stacie Woolard, Formal analysis; Paul Thomas, Methodology, Writing - review and editing; Peter Vogel, Data curation, Formal analysis, Visualization, Methodology, Writing - original draft, Writing - review and editing; Amber M Smith, Conceptualization, Resources, Data curation, Software, Formal analysis, Supervision, Funding acquisition, Validation, Investigation, Visualization, Methodology, Writing - original draft, Writing - review and editing

Author ORCIDs

Amber M Smith (iD) https://orcid.org/0000-0002-7092-6904

Ethics

Animal experimentation: All experimental procedures were performed under protocols O2A-020 or 17-096 approved by the Animal Care and Use Committees at St. Jude Children's Research Hospital (SJCRH) or the University of Tennessee Health Science Center (UTHSC), respectively, under relevant institutional and American Veterinary Medical Association (AVMA) guidelines. All experimental procedures were performed in a biosafety level 2 facility that is accredited by the American Association for Laboratory Animal Science (AALAS).

Decision letter and Author response

Decision letter https://doi.org/10.7554/eLife.68864.sa1
Author response https://doi.org/10.7554/eLife.68864.sa2

Additional files

Supplementary files

- Source data 1. Source data including viral titers, CD8$^+$ T cells, inflammation, lesion, and weight loss.

- Source code 1. Source code files for reproduction of all figures.

- Supplementary file 1. Statistical comparison of alternate models. Comparison of the Akaike Information Criteria (AIC) of the CD8$^+$ T cell model in *Equation (1)-(6)*, the alternate model in *Equation (A1)-(A6)*, and the Baral model in *Equation (A7)-(A8)*. The fit of these models is shown in *Appendix 1—figure 1*.

- Supplementary file 2. CD8 T cell depletion model parameters. Parameters, SSR, and AIC$_C$ obtained from fitting the CD8$^+$ T cell model (*Equation (1)-(6)*) to viral titers and CD8$^+$ T cells from mice infected with 75 TCID$_{50}$ PR8 and with CD8$^+$ T cells depleted at -2 d, 0 d, 3 d, and 7 d pi. The total number of CD8$^+$ T cells is $\hat{E} = E + E_M + \hat{E}_0$, where $\hat{E}_0 = 5.6 \times 10^3 \text{ cells}$, and all other parameters are those in *Table 1*. The best model is bolded.

- Transparent reporting form

Data availability

All data generated or analyzed during this study are included in the manuscript and supporting files. Source data files have been provided.

References

Ahmed H, Moore J, Manicassamy B, Garcia-Sastre A, Handel A, Antia R. 2017. Mathematical analysis of a mouse experiment suggests little role for resource depletion in controlling influenza infection within host. *arXiv*. https://arxiv.org/abs/1705.02565.

Ai T, Yang Z, Hou H, Zhan C, Chen C, Lv W, Tao Q, Sun Z, Xia L. 2020. Correlation of chest CT and RT-PCR testing for coronavirus disease 2019 (COVID-19) in China: a report of 1014 cases. *Radiology* **296**:E32–E40. DOI: https://doi.org/10.1148/radiol.2020200642, PMID: 32101510

Ajlan AM, Quiney B, Nicolaou S, Müller NL. 2009. Swine-origin influenza A (H1N1) viral infection: radiographic and CT findings. *American Journal of Roentgenology* **193**:1494–1499. DOI: https://doi.org/10.2214/AJR.09.3625, PMID: 19933639

Anderson KG, Sung H, Skon CN, Lefrancois L, Deisinger A, Vezys V, Masopust D. 2012. Cutting edge: intravascular staining redefines lung CD8 T cell responses. *The Journal of Immunology* **189**:2702–2706. DOI: https://doi.org/10.4049/jimmunol.1201682, PMID: 22896631

Baccam P, Beauchemin C, Macken CA, Hayden FG, Perelson AS. 2006. Kinetics of influenza A virus infection in humans. *Journal of Virology* **80**:7590–7599. DOI: https://doi.org/10.1128/JVI.01623-05, PMID: 16840338

Baloxavir Marboxil Investigators Group, Hayden FG, Sugaya N, Hirotsu N, Lee N, de Jong MD, Hurt AC, Ishida T, Sekino H, Yamada K, Portsmouth S, Kawaguchi K, Shishido T, Arai M, Tsuchiya K, Uehara T, Watanabe A. 2018. Baloxavir marboxil for uncomplicated influenza in adults and adolescents. *New England Journal of Medicine* **379**:913–923. DOI: https://doi.org/10.1056/NEJMoa1716197, PMID: 30184455

Baral S, Antia R, Dixit NM. 2019. A dynamical motif comprising the interactions between antigens and CD8 T cells may underlie the outcomes of viral infections. *PNAS* **116**:17393–17398. DOI: https://doi.org/10.1073/pnas.1902178116, PMID: 31413198

Bautista E, Chotpitayasunondh T, Gao Z, Harper SA, Shaw M, Uyeki TM, Zaki SR, Hayden FG, Hui DS, Kettner JD, Kumar A, Lim M, Shindo N, Penn C, Nicholson KG, Writing Committee of the WHO Consultation on Clinical Aspects of Pandemic (H1N1) 2009 Influenza. 2010. Clinical aspects of pandemic 2009 influenza A (H1N1) virus infection. *The New England Journal of Medicine* **362**:1708–1719. DOI: https://doi.org/10.1056/NEJMra1000449, PMID: 20445182

Beauchemin CA, Handel A. 2011. A review of mathematical models of influenza A infections within a host or cell culture: lessons learned and challenges ahead. *BMC Public Health* **11 Suppl 1**:S7. DOI: https://doi.org/10.1186/1471-2458-11-S1-S7, PMID: 21356136

Bedoui S, Gebhardt T. 2011. Interaction between dendritic cells and T cells during peripheral virus infections: a role for antigen presentation beyond lymphoid organs? *Current Opinion in Immunology* **23**:124–130. DOI: https://doi.org/10.1016/j.coi.2010.11.001, PMID: 21112755

Bender BS, Croghan T, Zhang L, Small PA. 1992. Transgenic mice lacking class I major histocompatibility complex-restricted T cells have delayed viral clearance and increased mortality after influenza virus challenge. *Journal of Experimental Medicine* **175**:1143–1145. DOI: https://doi.org/10.1084/jem.175.4.1143, PMID: 1552285

Boianelli A, Nguyen VK, Ebensen T, Schulze K, Wilk E, Sharma N, Stegemann-Koniszewski S, Bruder D, Toapanta FR, Guzmán CA, Meyer-Hermann M, Hernandez-Vargas EA. 2015. Modeling influenza virus infection: a roadmap for influenza research. *Viruses* **7**:5274–5304. DOI: https://doi.org/10.3390/v7102875, PMID: 26473911

Bonhoeffer S, Rembiszewski M, Ortiz GM, Nixon DF. 2000. Risks and benefits of structured antiretroviral drug therapy interruptions in HIV-1 infection. *Aids* **14**:2313–2322. DOI: https://doi.org/10.1097/00002030-200010200-00012, PMID: 11089619

Boon AC, Finkelstein D, Zheng M, Liao G, Allard J, Klumpp K, Webster R, Peltz G, Webby RJ. 2011. H5N1 influenza virus pathogenesis in genetically diverse mice is mediated at the level of viral load. *mBio* **2**:e00171. DOI: https://doi.org/10.1128/mBio.00171-11, PMID: 21896679

Bouvier NM, Lowen AC. 2010. Animal models for influenza virus pathogenesis and transmission. *Viruses* **2**:1530–1563. DOI: https://doi.org/10.3390/v20801530, PMID: 21442033

Boyd DF, Allen EK, Randolph AG, Guo XJ, Weng Y, Sanders CJ, Bajracharya R, Lee NK, Guy CS, Vogel P, Guan W, Li Y, Liu X, Novak T, Newhams MM, Fabrizio TP, Wohlgemuth N, Mourani PM, Wight TN, Schultz-Cherry S, et al. 2020. Exuberant fibroblast activity compromises lung function via ADAMTS4. *Nature* **587**:466–471. DOI: https://doi.org/10.1038/s41586-020-2877-5, PMID: 33116313

Byrd RH, Lu P, Nocedal J, Zhu C. 1995. A limited memory algorithm for bound constrained optimization. *SIAM Journal on Scientific Computing* **16**:1190–1208. DOI: https://doi.org/10.1137/0916069

Cairns BJ. 2008. *Pydde*. 0.2.2.

Cao P, Wang Z, Yan AW, McVernon J, Xu J, Heffernan JM, Kedzierska K, McCaw JM. 2016. On the role of CD8$^+$ T cells in determining recovery time from influenza virus infection. *Frontiers in Immunology* **7**:611. DOI: https://doi.org/10.3389/fimmu.2016.00611, PMID: 28066421

Caramalho I, Faroudi M, Padovan E, Müller S, Valitutti S. 2009. Visualizing CTL/melanoma cell interactions: multiple hits must be delivered for tumour cell annihilation. *Journal of Cellular and Molecular Medicine* **13**: 3834–3846. DOI: https://doi.org/10.1111/j.1582-4934.2008.00586.x, PMID: 19017355

Carrat F, Vergu E, Ferguson NM, Lemaitre M, Cauchemez S, Leach S, Valleron AJ. 2008. Time lines of infection and disease in human influenza: a review of volunteer challenge studies. *American Journal of Epidemiology* **167**:775–785. DOI: https://doi.org/10.1093/aje/kwm375, PMID: 18230677

Channappanavar R, Fehr AR, Vijay R, Mack M, Zhao J, Meyerholz DK, Perlman S. 2016. Dysregulated type I interferon and inflammatory Monocyte-Macrophage responses cause lethal pneumonia in SARS-CoV-Infected mice. *Cell Host & Microbe* **19**:181–193. DOI: https://doi.org/10.1016/j.chom.2016.01.007, PMID: 26867177

Chen X, Liu S, Goraya MU, Maarouf M, Huang S, Chen JL. 2018. Host immune response to influenza A virus infection. *Frontiers in Immunology* **9**:320. DOI: https://doi.org/10.3389/fimmu.2018.00320, PMID: 29556226

Conway JM, Perelson AS. 2015. Post-treatment control of HIV infection. *PNAS* **112**:5467–5472. DOI: https://doi.org/10.1073/pnas.1419162112, PMID: 25870266

Cross EW, Blain TJ, Mathew D, Kedl RM. 2019. Anti-CD8 monoclonal antibody-mediated depletion alters the phenotype and behavior of surviving CD8+ T cells. *PLOS ONE* **14**:e0211446. DOI: https://doi.org/10.1371/journal.pone.0211446, PMID: 30735510

De Boer RJ, Perelson AS. 1995. Towards a general function describing T cell proliferation. *Journal of Theoretical Biology* **175**:567–576. DOI: https://doi.org/10.1006/jtbi.1995.0165, PMID: 7475092

De Boer RJ, Perelson AS. 1998. Target cell limited and immune control models of HIV infection: a comparison. *Journal of Theoretical Biology* **190**:201–214. DOI: https://doi.org/10.1006/jtbi.1997.0548, PMID: 9514649

de Jong MD, Simmons CP, Thanh TT, Hien VM, Smith GJ, Chau TN, Hoang DM, Chau NV, Khanh TH, Dong VC, Qui PT, Cam BV, Ha doQ, Guan Y, Peiris JS, Chinh NT, Hien TT, Farrar J. 2006. Fatal outcome of human influenza A (H5N1) is associated with high viral load and hypercytokinemia. *Nature Medicine* **12**:1203–1207. DOI: https://doi.org/10.1038/nm1477, PMID: 16964257

Deguine J, Breart B, Lemaître F, Di Santo JP, Bousso P. 2010. Intravital imaging reveals distinct dynamics for natural killer and CD8(+) T cells during tumor regression. *Immunity* **33**:632–644. DOI: https://doi.org/10.1016/j.immuni.2010.09.016, PMID: 20951068

Dobrovolny HM, Reddy MB, Kamal MA, Rayner CR, Beauchemin CA. 2013. Assessing mathematical models of influenza infections using features of the immune response. *PLOS ONE* **8**:e57088. DOI: https://doi.org/10.1371/journal.pone.0057088, PMID: 23468916

Duan S, Meliopoulos VA, McClaren JL, Guo XZ, Sanders CJ, Smallwood HS, Webby RJ, Schultz-Cherry SL, Doherty PC, Thomas PG. 2015. Diverse heterologous primary infections radically alter immunodominance hierarchies and clinical outcomes following H7N9 influenza challenge in mice. *PLOS Pathogens* **11**:e1004642. DOI: https://doi.org/10.1371/journal.ppat.1004642, PMID: 25668410

Duan S, Thomas PG. 2016. Balancing immune protection and immune pathology by CD8(+) T-Cell responses to influenza infection. *Frontiers in Immunology* **7**:25. DOI: https://doi.org/10.3389/fimmu.2016.00025, PMID: 26904022

Dunster JL, Byrne HM, King JR. 2014. The resolution of inflammation: a mathematical model of neutrophil and macrophage interactions. *Bulletin of Mathematical Biology* **76**:1953–1980. DOI: https://doi.org/10.1007/s11538-014-9987-x, PMID: 25053556

Eccles R. 2005. Understanding the symptoms of the common cold and influenza. *The Lancet Infectious Diseases* **5**:718–725. DOI: https://doi.org/10.1016/S1473-3099(05)70270-X, PMID: 16253889

Eichelberger M, Allan W, Zijlstra M, Jaenisch R, Doherty PC. 1991. Clearance of influenza virus respiratory infection in mice lacking class I major histocompatibility complex-restricted CD8+ T cells. *Journal of Experimental Medicine* **174**:875–880. DOI: https://doi.org/10.1084/jem.174.4.875, PMID: 1919440

Fang M, Sigal LJ. 2005. Antibodies and CD8+ T cells are complementary and essential for natural resistance to a highly lethal cytopathic virus. *The Journal of Immunology* **175**:6829–6836. DOI: https://doi.org/10.4049/jimmunol.175.10.6829, PMID: 16272340

Feikin DR, Fu W, Park DE, Shi Q, Higdon MM, Baggett HC, Brooks WA, Deloria Knoll M, Hammitt LL, Howie SRC, Kotloff KL, Levine OS, Madhi SA, Scott JAG, Thea DM, Adrian PV, Antonio M, Awori JO, Baillie VL, DeLuca AN, et al. 2017. Is higher viral load in the upper respiratory tract associated with severe pneumonia? findings from the PERCH study. *Clinical Infectious Diseases* **64**:S337–S346. DOI: https://doi.org/10.1093/cid/cix148, PMID: 28575373

Gadhamsetty S, Marée AF, Beltman JB, de Boer RJ. 2014. A general functional response of cytotoxic T lymphocyte-mediated killing of target cells. *Biophysical Journal* **106**:1780–1791. DOI: https://doi.org/10.1016/j.bpj.2014.01.048, PMID: 24739177

Gallagher M, Brooke C, Ke R, Koelle K. 2018. Causes and consequences of spatial Within-Host viral spread. *Viruses* **10**:627. DOI: https://doi.org/10.3390/v10110627

Ganusov VV, Barber DL, De Boer RJ. 2011. Killing of targets by CD8 T cells in the mouse spleen follows the law of mass action. *PLOS ONE* **6**:e15959. DOI: https://doi.org/10.1371/journal.pone.0015959, PMID: 21283669

Gao R, Bhatnagar J, Blau DM, Greer P, Rollin DC, Denison AM, Deleon-Carnes M, Shieh WJ, Sambhara S, Tumpey TM, Patel M, Liu L, Paddock C, Drew C, Shu Y, Katz JM, Zaki SR. 2013. Cytokine and chemokine profiles in lung tissues from fatal cases of 2009 pandemic influenza A (H1N1): role of the host immune response in pathogenesis. *The American Journal of Pathology* **183**:1258–1268. DOI: https://doi.org/10.1016/j.ajpath.2013.06.023, PMID: 23938324

Gill JR, Sheng ZM, Ely SF, Guinee DG, Beasley MB, Suh J, Deshpande C, Mollura DJ, Morens DM, Bray M, Travis WD, Taubenberger JK. 2010. Pulmonary pathologic findings of fatal 2009 pandemic influenza A/H1N1 viral infections. *Archives of Pathology & Laboratory Medicine* **134**:235–243. DOI: https://doi.org/10.5858/134.2.235, PMID: 20121613

Granados A, Peci A, McGeer A, Gubbay JB. 2017. Influenza and rhinovirus viral load and disease severity in upper respiratory tract infections. *Journal of Clinical Virology* **86**:14–19. DOI: https://doi.org/10.1016/j.jcv.2016.11.008, PMID: 27893998

Graw F, Regoes RR. 2009. Investigating CTL mediated killing with a 3D cellular automaton. *PLOS Computational Biology* **5**:e1000466. DOI: https://doi.org/10.1371/journal.pcbi.1000466, PMID: 19696876

Gubareva LV, Kaiser L, Hayden FG. 2000. Influenza virus neuraminidase inhibitors. *The Lancet* **355**:827–835. DOI: https://doi.org/10.1016/S0140-6736(99)11433-8, PMID: 10711940

Halle S, Keyser KA, Stahl FR, Busche A, Marquardt A, Zheng X, Galla M, Heissmeyer V, Heller K, Boelter J, Wagner K, Bischoff Y, Martens R, Braun A, Werth K, Uvarovskii A, Kempf H, Meyer-Hermann M, Arens R, Kremer M, et al. 2016. In Vivo Killing Capacity of Cytotoxic T Cells Is Limited and Involves Dynamic Interactions and T Cell Cooperativity. *Immunity* **44**:233–245. DOI: https://doi.org/10.1016/j.immuni.2016.01.010, PMID: 26872694

Han A, Poon JL, Powers JH, Leidy NK, Yu R, Memoli MJ. 2018. Using the influenza Patient-reported outcome (FLU-PRO) diary to evaluate symptoms of influenza viral infection in a healthy human challenge model. *BMC Infectious Diseases* **18**:353. DOI: https://doi.org/10.1186/s12879-018-3220-8, PMID: 30055573

Handel A, Liao LE, Beauchemin CAA. 2018. Progress and trends in mathematical modelling of influenza A virus infections. *Current Opinion in Systems Biology* **12**:30–36. DOI: https://doi.org/10.1016/j.coisb.2018.08.009

Harrington LE, Galvan M, Baum LG, Altman JD, Ahmed R. 2000. Differentiating between memory and effector CD8 T cells by altered expression of cell surface O-glycans. *Journal of Experimental Medicine* **191**:1241–1246. DOI: https://doi.org/10.1084/jem.191.7.1241, PMID: 10748241

Holder BP, Beauchemin CA. 2011. Exploring the effect of biological delays in kinetic models of influenza within a host or cell culture. *BMC Public Health* **11 Suppl 1**:S10. DOI: https://doi.org/10.1186/1471-2458-11-S1-S10, PMID: 21356129

Hou S, Doherty PC, Zijlstra M, Jaenisch R, Katz JM. 1992. Delayed clearance of Sendai virus in mice lacking class I MHC-restricted CD8 T cells. *Journal of Immunology* **149**:1319–1325. PMID: 1354233

Huang CT, Hung CY, Chen TC, Lin CY, Lin YC, Chang CS, He YC, Huang YL, Dutta A. 2017. Rapamycin adjuvant and exacerbation of severe influenza in an experimental mouse model. *Scientific Reports* **7**:4136. DOI: https://doi.org/10.1038/s41598-017-04365-6, PMID: 28646236

Iwasaki A, Medzhitov R. 2010. Regulation of adaptive immunity by the innate immune system. *Science* **327**:291–295. DOI: https://doi.org/10.1126/science.1183021

Iwasaki A, Medzhitov R. 2015. Control of adaptive immunity by the innate immune system. *Nature Immunology* **16**:343–353. DOI: https://doi.org/10.1038/ni.3123, PMID: 25789684

Iwasaki T, Nozima T. 1977. Defense mechanisms against primary influenza virus infection in mice: I. the roles of interferon and neutralizing antibodies and Thymus dependence of interferon and antibody production. *Journal of Immunology* **118**:256–263. PMID: 401512

Jain A, Pasare C. 2017. Innate control of adaptive immunity: beyond the Three-Signal paradigm. *The Journal of Immunology* **198**:3791–3800. DOI: https://doi.org/10.4049/jimmunol.1602000, PMID: 28483987

Jones AT, Federsppiel B, Ellies LG, Williams MJ, Burgener R, Duronio V, Smith CA, Takei F, Ziltener HJ. 1994. Characterization of the activation-associated isoform of CD43 on murine T lymphocytes. *Journal of Immunology* **153**:3426–3439. PMID: 7523493

Kaech SM, Hemby S, Kersh E, Ahmed R. 2002. Molecular and functional profiling of memory CD8 T cell differentiation. *Cell* **111**:837–851. DOI: https://doi.org/10.1016/S0092-8674(02)01139-X, PMID: 12526810

Kang SS, Herz J, Kim JV, Nayak D, Stewart-Hutchinson P, Dustin ML, McGavern DB. 2011. Migration of cytotoxic lymphocytes in cell cycle permits local MHC I-dependent control of division at sites of viral infection. *Journal of Experimental Medicine* **208**:747–759. DOI: https://doi.org/10.1084/jem.20101295, PMID: 21464219

Karlsson EA, Meliopoulos VA, Savage C, Livingston B, Mehle A, Schultz-Cherry S. 2015. Visualizing real-time influenza virus infection, transmission and protection in ferrets. *Nature Communications* **6**:6378. DOI: https://doi.org/10.1038/ncomms7378, PMID: 25744559

Keating R, Morris MY, Yue W, Reynolds CE, Harris TL, Brown SA, Doherty PC, Thomas PG, McGargill MA. 2018. Potential killers exposed: tracking endogenous influenza-specific CD8$^+$ T cells. *Immunology and Cell Biology* **96**:1104–1119. DOI: https://doi.org/10.1111/imcb.12189, PMID: 29972699

Kohr JR, Bhargava P, Takasugi J, Goodman RB, Medverd JR. 2010. Imaging appearance of swine-origin influenza A (novel 2009 H1N1) pneumonia in an immunocompromised patient. *Radiology Case Reports* **5**:361. DOI: https://doi.org/10.2484/rcr.v5i1.361, PMID: 27307850

Koshimichi H, Ishibashi T, Kawaguchi N, Sato C, Kawasaki A, Wajima T. 2018. Safety, tolerability, and pharmacokinetics of the novel Anti-influenza agent baloxavir marboxil in healthy adults: phase I study findings. *Clinical Drug Investigation* **38**:1189–1196. DOI: https://doi.org/10.1007/s40261-018-0710-9, PMID: 30288682

Kreijtz JH, Fouchier RA, Rimmelzwaan GF. 2011. Immune responses to influenza virus infection. *Virus Research* **162**:19–30. DOI: https://doi.org/10.1016/j.virusres.2011.09.022, PMID: 21963677

Kugel D, Kochs G, Obojes K, Roth J, Kobinger GP, Kobasa D, Haller O, Staeheli P, von Messling V. 2009. Intranasal administration of alpha interferon reduces seasonal influenza A virus morbidity in ferrets. *Journal of Virology* **83**:3843–3851. DOI: https://doi.org/10.1128/JVI.02453-08, PMID: 19193792

La Gruta NL, Kedzierska K, Stambas J, Doherty PC. 2007. A question of self-preservation: immunopathology in influenza virus infection. *Immunology & Cell Biology* **85**:85–92. DOI: https://doi.org/10.1038/sj.icb.7100026, PMID: 17213831

La Gruta NL, Turner SJ. 2014. T cell mediated immunity to influenza: mechanisms of viral control. *Trends in Immunology* **35**:396–402. DOI: https://doi.org/10.1016/j.it.2014.06.004, PMID: 25043801

Lambert Emo K, Hyun YM, Reilly E, Barilla C, Gerber S, Fowell D, Kim M, Topham DJ. 2016. Live imaging of influenza infection of the Trachea reveals dynamic regulation of CD8+ T cell motility by antigen. *PLOS Pathogens* **12**:e1005881. DOI: https://doi.org/10.1371/journal.ppat.1005881, PMID: 27644089

Lauder SN, Taylor PR, Clark SR, Evans RL, Hindley JP, Smart K, Leach H, Kidd EJ, Broadley KJ, Jones SA, Wise MP, Godkin AJ, O'Donnell V, Gallimore AM. 2011. Paracetamol reduces influenza-induced immunopathology in a mouse model of infection without compromising virus clearance or the generation of protective immunity. *Thorax* **66**:368–374. DOI: https://doi.org/10.1136/thx.2010.150318, PMID: 21310755

Lawrence CW, Ream RM, Braciale TJ. 2005. Frequency, specificity, and sites of expansion of CD8+ T cells during primary pulmonary influenza virus infection. *The Journal of Immunology* **174**:5332–5340. DOI: https://doi.org/10.4049/jimmunol.174.9.5332, PMID: 15843530

Le D, Miller JD, Ganusov VV. 2014. Mathematical modeling provides kinetic details of the human immune response to vaccination. *Frontiers in Cellular and Infection Microbiology* **4**:177. DOI: https://doi.org/10.3389/fcimb.2014.00177, PMID: 25621280

Le Bon A, Tough DF. 2002. Links between innate and adaptive immunity via type I interferon. *Current Opinion in Immunology* **14**:432–436. DOI: https://doi.org/10.1016/S0952-7915(02)00354-0, PMID: 12088676

Lee HY, Topham DJ, Park SY, Hollenbaugh J, Treanor J, Mosmann TR, Jin X, Ward BM, Miao H, Holden-Wiltse J, Perelson AS, Zand M, Wu H. 2009. Simulation and prediction of the adaptive immune response to influenza A virus infection. *Journal of Virology* **83**:7151–7165. DOI: https://doi.org/10.1128/JVI.00098-09, PMID: 19439465

Lee CS, Lee JH. 2010. Dynamics of clinical symptoms in patients with pandemic influenza A (H1N1). *Clinical Microbiology and Infection* **16**:389–390. DOI: https://doi.org/10.1111/j.1469-0691.2010.03117.x, PMID: 20222893

Levin D, Forrest S, Banerjee S, Clay C, Cannon J, Moses M, Koster F. 2016. A spatial model of the efficiency of T cell search in the influenza-infected lung. *Journal of Theoretical Biology* **398**:52–63. DOI: https://doi.org/10.1016/j.jtbi.2016.02.022, PMID: 26920246

Li P, Su DJ, Zhang JF, Xia XD, Sui H, Zhao DH. 2011. Pneumonia in novel swine-origin influenza A (H1N1) virus infection: high-resolution CT findings. *European Journal of Radiology* **80**:e146–e152. DOI: https://doi.org/10.1016/j.ejrad.2010.05.029, PMID: 20566254

Li P, Zhang JF, Xia XD, Su DJ, Liu BL, Zhao DL, Liu Y, Zhao DH. 2012. Serial evaluation of high-resolution CT findings in patients with pneumonia in novel swine-origin influenza A (H1N1) virus infection. *The British Journal of Radiology* **85**:729–735. DOI: https://doi.org/10.1259/bjr/85580974, PMID: 22167502

Li Y, Handel A. 2014. Modeling inoculum dose dependent patterns of acute virus infections. *Journal of Theoretical Biology* **347**:63–73. DOI: https://doi.org/10.1016/j.jtbi.2014.01.008, PMID: 24440713

Lu J, Duan X, Zhao W, Wang J, Wang H, Zhou K, Fang M. 2018. Aged mice are more resistant to influenza virus infection due to reduced inflammation and lung pathology. *Aging and Disease* **9**:358. DOI: https://doi.org/10.14336/AD.2017.0701, PMID: 29896425

Luker KE, Luker GD. 2010. Bioluminescence imaging of reporter mice for studies of infection and inflammation. *Antiviral Research* **86**:93–100. DOI: https://doi.org/10.1016/j.antiviral.2010.02.002, PMID: 20417377

Luster AD. 2002. The role of chemokines in linking innate and adaptive immunity. *Current Opinion in Immunology* **14**:129–135. DOI: https://doi.org/10.1016/S0952-7915(01)00308-9

Manchanda H, Seidel N, Krumbholz A, Sauerbrei A, Schmidtke M, Guthke R. 2014. Within-host influenza dynamics: a small-scale mathematical modeling approach. *Biosystems* **118**:51–59. DOI: https://doi.org/10.1016/j.biosystems.2014.02.004, PMID: 24614233

Manicassamy B, Manicassamy S, Belicha-Villanueva A, Pisanelli G, Pulendran B, García-Sastre A. 2010. Analysis of in vivo dynamics of influenza virus infection in mice using a GFP reporter virus. *PNAS* **107**:11531–11536. DOI: https://doi.org/10.1073/pnas.0914994107, PMID: 20534532

Marathe BM, Wong SS, Vogel P, Garcia-Alcalde F, Webster RG, Webby RJ, Najera I, Govorkova EA. 2016. Combinations of oseltamivir and T-705 extend the treatment window for highly pathogenic influenza A(H5N1) Virus infection in mice. *Scientific Reports* **6**:26742. DOI: https://doi.org/10.1038/srep26742, PMID: 27221530

Marathe BM, Mostafa HH, Vogel P, Pascua PNQ, Jones JC, Russell CJ, Webby RJ, Govorkova EA. 2017. A pharmacologically immunosuppressed mouse model for assessing influenza B virus pathogenicity and oseltamivir treatment. *Antiviral Research* **148**:20–31. DOI: https://doi.org/10.1016/j.antiviral.2017.10.021, PMID: 29100887

Margine I, Krammer F. 2014. Animal models for influenza viruses: implications for universal vaccine development. *Pathogens* **3**:845–874. DOI: https://doi.org/10.3390/pathogens3040845, PMID: 25436508

Matheu MP, Teijaro JR, Walsh KB, Greenberg ML, Marsolais D, Parker I, Rosen H, Oldstone MB, Cahalan MD. 2013. Three phases of CD8 T cell response in the lung following H1N1 influenza infection and sphingosine 1 phosphate agonist therapy. *PLOS ONE* **8**:e58033. DOI: https://doi.org/10.1371/journal.pone.0058033, PMID: 23533579

Mauad T, Hajjar LA, Callegari GD, da Silva LF, Schout D, Galas FR, Alves VA, Malheiros DM, Auler JO, Ferreira AF, Borsato MR, Bezerra SM, Gutierrez PS, Caldini ET, Pasqualucci CA, Dolhnikoff M, Saldiva PH. 2010. Lung pathology in fatal novel human influenza A (H1N1) infection. *American Journal of Respiratory and Critical Care Medicine* **181**:72–79. DOI: https://doi.org/10.1164/rccm.200909-1420OC, PMID: 19875682

McAuley JL, Hornung F, Boyd KL, Smith AM, McKeon R, Bennink J, Yewdell JW, McCullers JA. 2007. Expression of the 1918 influenza A virus PB1-F2 enhances the pathogenesis of viral and secondary bacterial pneumonia. *Cell Host & Microbe* **2**:240–249. DOI: https://doi.org/10.1016/j.chom.2007.09.001, PMID: 18005742

McGill J, Legge KL. 2009. Cutting edge: contribution of lung-resident T cell proliferation to the overall magnitude of the antigen-specific CD8 T cell response in the lungs following murine influenza virus infection. *The Journal of Immunology* **183**:4177–4181. DOI: https://doi.org/10.4049/jimmunol.0901109, PMID: 19767567

McMichael AJ, Gotch FM, Noble GR, Beare PA. 1983. Cytotoxic T-cell immunity to influenza. *New England Journal of Medicine* **309**:13–17. DOI: https://doi.org/10.1056/NEJM198307073090103, PMID: 6602294

Medina RA, García-Sastre A. 2011. Influenza A viruses: new research developments. *Nature Reviews Microbiology* **9**:590–603. DOI: https://doi.org/10.1038/nrmicro2613, PMID: 21747392

Memoli MJ, Athota R, Reed S, Czajkowski L, Bristol T, Proudfoot K, Hagey R, Voell J, Fiorentino C, Ademposi A, Shoham S, Taubenberger JK. 2014. The natural history of influenza infection in the severely immunocompromised vs nonimmunocompromised hosts. *Clinical Infectious Diseases* **58**:214–224. DOI: https://doi.org/10.1093/cid/cit725, PMID: 24186906

Mempel TR, Pittet MJ, Khazaie K, Weninger W, Weissleder R, von Boehmer H, von Andrian UH. 2006. Regulatory T cells reversibly suppress cytotoxic T cell function independent of effector differentiation. *Immunity* **25**:129–141. DOI: https://doi.org/10.1016/j.immuni.2006.04.015, PMID: 16860762

Merrill SJ. 1982. Foundations of the use of an enzyme-kinetic analogy in cell-mediated cytotoxicity. *Mathematical Biosciences* **62**:219–235. DOI: https://doi.org/10.1016/0025-5564(82)90084-0

Mestas J, Hughes CC. 2004. Of mice and not men: differences between mouse and human immunology. *The Journal of Immunology* **172**:2731–2738. DOI: https://doi.org/10.4049/jimmunol.172.5.2731, PMID: 14978070

Miao H, Hollenbaugh JA, Zand MS, Holden-Wiltse J, Mosmann TR, Perelson AS, Wu H, Topham DJ. 2010. Quantifying the early immune response and adaptive immune response kinetics in mice infected with influenza A virus. *Journal of Virology* **84**:6687–6698. DOI: https://doi.org/10.1128/JVI.00266-10, PMID: 20410284

Monto AS, Gravenstein S, Elliott M, Colopy M, Schweinle J. 2000. Clinical signs and symptoms predicting influenza infection. *Archives of Internal Medicine* **160**:3243–3247. DOI: https://doi.org/10.1001/archinte.160.21.3243, PMID: 11088084

Moscona A. 2005. Neuraminidase inhibitors for influenza. *New England Journal of Medicine* **353**:1363–1373. DOI: https://doi.org/10.1056/NEJMra050740, PMID: 16192481

Moskophidis D, Kioussis D. 1998. Contribution of virus-specific CD8+ cytotoxic T cells to virus clearance or pathologic manifestations of influenza virus infection in a T cell receptor transgenic mouse model. *Journal of Experimental Medicine* **188**:223–232. DOI: https://doi.org/10.1084/jem.188.2.223, PMID: 9670035

Müller V, Marée AFM, De Boer RJ. 2001. Small variations in multiple parameters account for wide variations in HIV–1 set–points: a novel modelling approach. *Proceedings of the Royal Society of London. Series B: Biological Sciences* **268**:235–242. DOI: https://doi.org/10.1098/rspb.2000.1358

Music N, Reber AJ, Lipatov AS, Kamal RP, Blanchfield K, Wilson JR, Donis RO, Katz JM, York IA. 2014. Influenza vaccination accelerates recovery of ferrets from lymphopenia. *PLOS ONE* **9**:e100926. DOI: https://doi.org/10.1371/journal.pone.0100926, PMID: 24968319

Onami TM, Harrington LE, Williams MA, Galvan M, Larsen CP, Pearson TC, Manjunath N, Baum LG, Pearce BD, Ahmed R. 2002. Dynamic regulation of T cell immunity by CD43. *Journal of Immunology* **168**:6022–6031. DOI: https://doi.org/10.4049/jimmunol.168.12.6022, PMID: 12055210

Ostler T, Davidson W, Ehl S. 2002. Virus clearance and immunopathology by CD8(+) T cells during infection with respiratory syncytial virus are mediated by IFN-gamma. *European Journal of Immunology* **32**:2117–2123. DOI: https://doi.org/10.1002/1521-4141(200208)32:8<2117::AID-IMMU2117>3.0.CO;2-C, PMID: 12209623

Parzych EM, DiMenna LJ, Latimer BP, Small JC, Kannan S, Manson B, Lasaro MO, Wherry EJ, Ertl HC. 2013. Influenza virus specific CD8+ T cells exacerbate infection following high dose influenza challenge of aged mice. *BioMed Research International* **2013**:876314. DOI: https://doi.org/10.1155/2013/876314, PMID: 24187666

Perelson AS, Bell GI. 1982. Delivery of lethal hits by cytotoxic T lymphocytes in multicellular conjugates occurs sequentially but at random times. *Journal of Immunology* **129**:2796–2801. PMID: 6982942

Perry M. 2018. *Simanneal*. 0.4.1.

Pilyugin SS, Antia R. 2000. Modeling immune responses with handling time. *Bulletin of Mathematical Biology* **62**: 869–890. DOI: https://doi.org/10.1006/bulm.2000.0181, PMID: 11016088

Price I, Mochan-Keef ED, Swigon D, Ermentrout GB, Lukens S, Toapanta FR, Ross TM, Clermont G. 2015. The inflammatory response to influenza A virus (H1N1): An experimental and mathematical study. *Journal of Theoretical Biology* **374**:83–93. DOI: https://doi.org/10.1016/j.jtbi.2015.03.017, PMID: 25843213

Ramirez-Zuniga I, Rubin JE, Swigon D, Clermont G. 2019. Mathematical modeling of energy consumption in the acute inflammatory response. *Journal of Theoretical Biology* **460**:101–114. DOI: https://doi.org/10.1016/j.jtbi. 2018.08.033, PMID: 30149010

Reed LJ, Muench H. 1938. A simple method of estimating fifty per cent endpoints12. *American Journal of Epidemiology* **27**:493–497. DOI: https://doi.org/10.1093/oxfordjournals.aje.a118408

Reynolds A, Rubin J, Clermont G, Day J, Vodovotz Y, Bard Ermentrout G. 2006. A reduced mathematical model of the acute inflammatory response: I. Derivation of model and analysis of anti-inflammation. *Journal of Theoretical Biology* **242**:220–236. DOI: https://doi.org/10.1016/j.jtbi.2006.02.016, PMID: 16584750

Russell DG, Cardona PJ, Kim MJ, Allain S, Altare F. 2009. Foamy macrophages and the progression of the human tuberculosis granuloma. *Nature Immunology* **10**:943. DOI: https://doi.org/10.1038/ni.1781, PMID: 196 92995

Ruuskanen O, Lahti E, Jennings LC, Murdoch DR. 2011. Viral pneumonia. *Lancet* **377**:1264–1275. DOI: https:// doi.org/10.1016/S0140-6736(10)61459-6, PMID: 21435708

Rygiel TP, Rijkers ES, de Ruiter T, Stolte EH, van der Valk M, Rimmelzwaan GF, Boon L, van Loon AM, Coenjaerts FE, Hoek RM, Tesselaar K, Meyaard L. 2009. Lack of CD200 enhances pathological T cell responses during influenza infection. *The Journal of Immunology* **183**:1990–1996. DOI: https://doi.org/10.4049/jimmunol. 0900252, PMID: 19587022

Sartorius A, Lu Q, Vieira S, Tonnellier M, Lenaour G, Goldstein I, Rouby JJ. 2007. Mechanical ventilation and lung infection in the genesis of air-space enlargement. *Critical Care* **11**:R14. DOI: https://doi.org/10.1186/ cc5680, PMID: 17274806

Shieh WJ, Blau DM, Denison AM, Deleon-Carnes M, Adem P, Bhatnagar J, Sumner J, Liu L, Patel M, Batten B, Greer P, Jones T, Smith C, Bartlett J, Montague J, White E, Rollin D, Gao R, Seales C, Jost H, et al. 2010. 2009 pandemic influenza A (H1N1): pathology and pathogenesis of 100 fatal cases in the United States. *The American Journal of Pathology* **177**:166–175. DOI: https://doi.org/10.2353/ajpath.2010.100115, PMID: 2050 8031

Simonsen L, Fukuda K, Schonberger LB, Cox NJ. 2000. The impact of influenza epidemics on hospitalizations. *The Journal of Infectious Diseases* **181**:831–837. DOI: https://doi.org/10.1086/315320, PMID: 10720501

Slütter B, Van Braeckel-Budimir N, Abboud G, Varga SM, Salek-Ardakani S, Harty JT. 2017. Dynamics of influenza-induced lung-resident memory T cells underlie waning heterosubtypic immunity. *Science Immunology* **2**:eaag2031. DOI: https://doi.org/10.1126/sciimmunol.aag2031, PMID: 28783666

Smith AM, Adler FR, Perelson AS. 2010. An accurate two-phase approximate solution to an acute viral infection model. *Journal of Mathematical Biology* **60**:711–726. DOI: https://doi.org/10.1007/s00285-009-0281-8, PMID: 19633852

Smith AM, Adler FR, McAuley JL, Gutenkunst RN, Ribeiro RM, McCullers JA, Perelson AS. 2011a. Effect of 1918 PB1-F2 expression on influenza A virus infection kinetics. *PLOS Computational Biology* **7**:e1001081. DOI: https://doi.org/10.1371/journal.pcbi.1001081, PMID: 21379324

Smith AM, McCullers JA, Adler FR. 2011b. Mathematical model of a three-stage innate immune response to a pneumococcal lung infection. *Journal of Theoretical Biology* **276**:106–116. DOI: https://doi.org/10.1016/j.jtbi. 2011.01.052, PMID: 21300073

Smith AM, Adler FR, Ribeiro RM, Gutenkunst RN, McAuley JL, McCullers JA, Perelson AS. 2013. Kinetics of coinfection with influenza A virus and *Streptococcus pneumoniae*. *PLOS Pathogens* **9**:e1003238. DOI: https:// doi.org/10.1371/journal.ppat.1003238, PMID: 23555251

Smith AP, Moquin DJ, Bernhauerova V, Smith AM. 2018. Influenza Virus Infection Model With Density Dependence Supports Biphasic Viral Decay. *Frontiers in Microbiology* **9**:1554. DOI: https://doi.org/10.3389/ fmicb.2018.01554, PMID: 30042759

Smith AM. 2018a. Validated models of immune response to virus infection. *Current Opinion in Systems Biology* **12**:46–52. DOI: https://doi.org/10.1016/j.coisb.2018.10.005, PMID: 31723715

Smith AM. 2018b. Host-pathogen kinetics during influenza infection and coinfection: insights from predictive modeling. *Immunological Reviews* **285**:97–112. DOI: https://doi.org/10.1111/imr.12692, PMID: 30129197

Smith CA, Kulkarni U, Chen J, Goldstein DR. 2019. Influenza virus inoculum volume is critical to elucidate age-dependent mortality in mice. *Aging Cell* **18**:e12893. DOI: https://doi.org/10.1111/acel.12893, PMID: 30632262

Smith AM, McCullers JA. 2014. Secondary bacterial infections in influenza virus infection pathogenesis. *Current Topics in Microbiology and Immunology* **385**:327–356. DOI: https://doi.org/10.1007/82_2014_394, PMID: 25027822

Smith AM, Perelson AS. 2011. Influenza A virus infection kinetics: quantitative data and models. *Wiley Interdisciplinary Reviews: Systems Biology and Medicine* **3**:429–445. DOI: https://doi.org/10.1002/wsbm.129, PMID: 21197654

Soto-Abraham MV, Soriano-Rosas J, Díaz-Quiñónez A, Silva-Pereyra J, Vazquez-Hernandez P, Torres-López O, Roldán A, Cruz-Gordillo A, Alonso-Viveros P, Navarro-Reynoso F. 2009. Pathological changes associated with

the 2009 H1N1 virus. *New England Journal of Medicine* **361**:2001–2003. DOI: https://doi.org/10.1056/NEJMc0907171

Srivastava B, Błazejewska P, Hessmann M, Bruder D, Geffers R, Mauel S, Gruber AD, Schughart K. 2009. Host genetic background strongly influences the response to influenza a virus infections. *PLOS ONE* **4**:e4857. DOI: https://doi.org/10.1371/journal.pone.0004857, PMID: 19293935

Sun J, Madan R, Karp CL, Braciale TJ. 2009. Effector T cells control lung inflammation during acute influenza virus infection by producing IL-10. *Nature Medicine* **15**:277–284. DOI: https://doi.org/10.1038/nm.1929, PMID: 19234462

Szretter KJ, Gangappa S, Belser JA, Zeng H, Chen H, Matsuoka Y, Sambhara S, Swayne DE, Tumpey TM, Katz JM. 2009. Early control of H5N1 influenza virus replication by the type I interferon response in mice. *Journal of Virology* **83**:5825–5834. DOI: https://doi.org/10.1128/JVI.02144-08, PMID: 19297490

Tang BM, Shojaei M, Teoh S, Meyers A, Ho J, Ball TB, Keynan Y, Pisipati A, Kumar A, Eisen DP, Lai K, Gillett M, Santram R, Geffers R, Schreiber J, Mozhui K, Huang S, Parnell GP, Nalos M, Holubova M, et al. 2019. Neutrophils-related host factors associated with severe disease and fatality in patients with influenza infection. *Nature Communications* **10**:3422. DOI: https://doi.org/10.1038/s41467-019-11249-y, PMID: 31366921

Taubenberger JK, Morens DM. 2008. The pathology of influenza virus infections. *Annual Review of Pathology: Mechanisms of Disease* **3**:499–522. DOI: https://doi.org/10.1146/annurev.pathmechdis.3.121806.154316, PMID: 18039138

Thangavel RR, Bouvier NM. 2014. Animal models for influenza virus pathogenesis, transmission, and immunology. *Journal of Immunological Methods* **410**:60–79. DOI: https://doi.org/10.1016/j.jim.2014.03.023, PMID: 24709389

Thompson WW, Shay DK, Weintraub E, Brammer L, Bridges CB, Cox NJ, Fukuda K. 2004. Influenza-associated hospitalizations in the united states. *Jama* **292**:1333–1340. DOI: https://doi.org/10.1001/jama.292.11.1333, PMID: 15367555

Toapanta FR, Ross TM. 2009. Impaired immune responses in the lungs of aged mice following influenza infection. *Respiratory Research* **10**:112. DOI: https://doi.org/10.1186/1465-9921-10-112, PMID: 19922665

Toniolo Neto J. 2014. Neuraminidase inhibitors for preventing and treating influenza in healthy adults and children. *Sao Paulo Medical Journal* **132**:256–257. DOI: https://doi.org/10.1590/1516-3180.20141324T2, PMID: 25055075

Trammell RA, Toth LA. 2011. Markers for predicting death as an outcome for mice used in infectious disease research. *Comparative Medicine* **61**:492–498. PMID: 22330575

Tran V, Moser LA, Poole DS, Mehle A. 2013. Highly sensitive real-time in vivo imaging of an influenza reporter virus reveals dynamics of replication and spread. *Journal of Virology* **87**:13321–13329. DOI: https://doi.org/10.1128/JVI.02381-13, PMID: 24089552

Treanor JJ, Hayden FG, Vrooman PS, Barbarash R, Bettis R, Riff D, Singh S, Kinnersley N, Ward P, Mills RG. 2000. Efficacy and safety of the oral neuraminidase inhibitor oseltamivir in treating acute influenza: a randomized controlled trial. US Oral Neuraminidase Study Group. *JAMA* **283**:1016–1024. DOI: https://doi.org/10.1001/jama.283.8.1016, PMID: 10697061

Uddbäck I, Cartwright EK, Schøller AS, Wein AN, Hayward SL, Lobby J, Takamura S, Thomsen AR, Kohlmeier JE, Christensen JP. 2021. Long-term maintenance of lung resident memory T cells is mediated by persistent antigen. *Mucosal Immunology* **14**:92–99. DOI: https://doi.org/10.1038/s41385-020-0309-3, PMID: 32518368

Ulrichs T, Kosmiadi GA, Trusov V, Jörg S, Pradl L, Titukhina M, Mishenko V, Gushina N, Kaufmann SH. 2004. Human tuberculous granulomas induce peripheral lymphoid follicle-like structures to orchestrate local host defence in the lung. *The Journal of Pathology* **204**:217–228. DOI: https://doi.org/10.1002/path.1628, PMID: 15376257

Van Braeckel-Budimir N, Varga SM, Badovinac VP, Harty JT. 2018. Repeated Antigen Exposure Extends the Durability of Influenza-Specific Lung-Resident Memory CD8^{+} T Cells and Heterosubtypic Immunity. *Cell Reports* **24**:3374–3382. DOI: https://doi.org/10.1016/j.celrep.2018.08.073, PMID: 30257199

van de Sandt CE, Bárcena M, Koster AJ, Kasper J, Kirkpatrick CJ, Scott DP, de Vries RD, Herold S, Rimmelzwaan GF, Kuiken T, Short KR. 2017. Human CD8^{+} T Cells Damage Noninfected Epithelial Cells during Influenza Virus Infection In Vitro. *American Journal of Respiratory Cell and Molecular Biology* **57**:536–546. DOI: https://doi.org/10.1165/rcmb.2016-0377OC, PMID: 28613916

Wakim LM, Smith J, Caminschi I, Lahoud MH, Villadangos JA. 2015. Antibody-targeted vaccination to lung dendritic cells generates tissue-resident memory CD8 T cells that are highly protective against influenza virus infection. *Mucosal Immunology* **8**:1060–1071. DOI: https://doi.org/10.1038/mi.2014.133, PMID: 25586557

Wang Z, Wan Y, Qiu C, Quiñones-Parra S, Zhu Z, Loh L, Tian D, Ren Y, Hu Y, Zhang X, Thomas PG, Inouye M, Doherty PC, Kedzierska K, Xu J. 2015. Recovery from severe H7N9 disease is associated with diverse response mechanisms dominated by CD8^{+} T cells. *Nature Communications* **6**:6833. DOI: https://doi.org/10.1038/ncomms7833, PMID: 25967273

Watanabe S, Alexander M, Misharin AV, Budinger GRS. 2019. The role of macrophages in the resolution of inflammation. *The Journal of Clinical Investigation* **129**:2619–2628. DOI: https://doi.org/10.1172/JCI124615, PMID: 31107246

Weinfurter JT, Brunner K, Capuano SV, Li C, Broman KW, Kawaoka Y, Friedrich TC. 2011. Cross-reactive T cells are involved in rapid clearance of 2009 pandemic H1N1 influenza virus in nonhuman primates. *PLOS Pathogens* **7**:e1002381. DOI: https://doi.org/10.1371/journal.ppat.1002381, PMID: 22102819

Wells MA, Albrecht P, Ennis FA. 1981. Recovery from a viral respiratory infection. I. Influenza pneumonia in normal and T-deficient mice. *Journal of Immunology* **126**:1036–1041. PMID: 6970211

Wiedemann A, Depoil D, Faroudi M, Valitutti S. 2006. Cytotoxic T lymphocytes kill multiple targets simultaneously via spatiotemporal uncoupling of lytic and stimulatory synapses. *PNAS* **103**:10985–10990. DOI: https://doi.org/10.1073/pnas.0600651103, PMID: 16832064

Wilkinson TM, Li CK, Chui CS, Huang AK, Perkins M, Liebner JC, Lambkin-Williams R, Gilbert A, Oxford J, Nicholas B, Staples KJ, Dong T, Douek DC, McMichael AJ, Xu XN. 2012. Preexisting influenza-specific CD4+ T cells correlate with disease protection against influenza challenge in humans. *Nature Medicine* **18**:274–280. DOI: https://doi.org/10.1038/nm.2612, PMID: 22286307

Wong HYF, Lam HYS, Fong AH, Leung ST, Chin TW, Lo CSY, Lui MM, Lee JCY, Chiu KW, Chung TW, Lee EYP, Wan EYF, Hung IFN, Lam TPW, Kuo MD, Ng MY. 2020. Frequency and Distribution of Chest Radiographic Findings in Patients Positive for COVID-19. *Radiology* **296**:E72–E78. DOI: https://doi.org/10.1148/radiol.2020201160, PMID: 32216717

Wu H, Kumar A, Miao H, Holden-Wiltse J, Mosmann TR, Livingstone AM, Belz GT, Perelson AS, Zand MS, Topham DJ. 2011. Modeling of influenza-specific CD8+ T cells during the primary response indicates that the spleen is a major source of effectors. *Journal of Immunology* **187**:4474–4482. DOI: https://doi.org/10.4049/jimmunol.1101443, PMID: 21948988

Xu L, Yoon H, Zhao MQ, Liu J, Ramana CV, Enelow RI. 2004. Cutting edge: pulmonary immunopathology mediated by antigen-specific expression of TNF-alpha by antiviral CD8+ T cells. *Journal of Immunology* **173**:721–725. DOI: https://doi.org/10.4049/jimmunol.173.2.721, PMID: 15240656

Xue KS, Stevens-Ayers T, Campbell AP, Englund JA, Pergam SA, Boeckh M, Bloom JD. 2017. Parallel evolution of influenza across multiple spatiotemporal scales. *eLife* **6**:e26875. DOI: https://doi.org/10.7554/eLife.26875, PMID: 28653624

Yannelli JR, Sullivan JA, Mandell GL, Engelhard VH. 1986. Reorientation and fusion of cytotoxic T lymphocyte granules after interaction with target cells as determined by high resolution cinemicrography. *Journal of Immunology* **136**:377–382. PMID: 3510248

Yap KL, Ada GL. 1978. Cytotoxic T cells in the lungs of mice infected with an influenza A virus. *Scandinavian Journal of Immunology* **7**:73–80. DOI: https://doi.org/10.1111/j.1365-3083.1978.tb00428.x, PMID: 305613

Yates AJ, Van Baalen M, Antia R. 2011. Virus replication strategies and the critical CTL numbers required for the control of infection. *PLOS Computational Biology* **7**:e1002274. DOI: https://doi.org/10.1371/journal.pcbi.1002274, PMID: 22125483

Yoon H, Legge KL, Sung SS, Braciale TJ. 2007. Sequential activation of CD8+ T cells in the draining lymph nodes in response to pulmonary virus infection. *Journal of Immunology* **179**:391–399. DOI: https://doi.org/10.4049/jimmunol.179.1.391, PMID: 17579060

Zachariadis O, Cassidy JP, Brady J, Mahon BP. 2006. gammadelta T cells regulate the early inflammatory response to bordetella pertussis infection in the murine respiratory tract. *Infection and Immunity* **74**:1837–1845. DOI: https://doi.org/10.1128/IAI.74.3.1837-1845.2006, PMID: 16495558

Zagury D, Bernard J, Thierness N, Feldman M, Berke G. 1975. Isolation and characterization of individual functionally reactive cytotoxic T lymphocytes: conjugation, killing and recycling at the single cell level. *European Journal of Immunology* **5**:818–822. DOI: https://doi.org/10.1002/eji.1830051205

Zens KD, Chen JK, Farber DL. 2016. Vaccine-generated lung tissue–resident memory T cells provide heterosubtypic protection to influenza infection. *JCI Insight* **1**:e85832. DOI: https://doi.org/10.1172/jci.insight.85832

Zhang N, Bevan MJ. 2011. CD8(+) T cells: foot soldiers of the immune system. *Immunity* **35**:161–168. DOI: https://doi.org/10.1016/j.immuni.2011.07.010, PMID: 21867926

Zhu C, Byrd RH, Lu P, Nocedal J. 1997. Algorithm 778: L-BFGS-B: Fortran subroutines for large-scale bound-constrained optimization. *ACM T Math Software* **23**:550–560. DOI: https://doi.org/10.1145/279232.279236

Appendix 1

Alternate CD8⁺ T cell Models

We examined alternate formulations of the CD8⁺ T cell model to further investigate the density-dependence in the CD8⁺ T cell response. Rather than assuming that $CD8_E$-mediated clearance of infected cells is dependent on their density, the model in *Equation (A1)-(A6)* assumes that the rate of $CD8_E$ expansion is dependent on the density of infected cells. Similar models have been used to study CD8⁺ T cell responses during HIV infection (*Conway and Perelson, 2015*; *Bonhoeffer et al., 2000*) and other viral infections (*Baral et al., 2019*). The differences between this alternate model and the CD8⁺ T cell model (*Equation (1)-(6)*) are in bold.

$$\frac{dT}{dt} = -\beta TV \tag{A1}$$

$$\frac{dI_1}{dt} = \beta TV - kI_1 \tag{A2}$$

$$\frac{dI_2}{dt} = kI_1 - \delta I_2 - \boldsymbol{\delta_{Ea}E I_2} \tag{A3}$$

$$\frac{dV}{dt} = pI_2 - cV \tag{A4}$$

$$\frac{dE}{dt} = \frac{\boldsymbol{\eta_{Ea}}}{\boldsymbol{K_{Ea} + I_2}} I_2(t - \tau_E) - d_E E \tag{A5}$$

$$\frac{dE_M}{dt} = \zeta E(t - \tau_M) \tag{A6}$$

When a linear $CD8_E$-mediated infected cell clearance rate is included, the $CD8_E$ dynamics between 3–5 d pi cannot be replicated and returned a statistically worse fit via AIC (*Supplementary file 1*). However, because these cells may not have effector functions and contribute to infected cell clearance at this time (see Discussion), we excluded these data and the term $\xi I_2/(K_E + E)$ when fitting *Equation (A1)-(A6)* to the viral load and total CD8⁺ T cell data (*Appendix 1—figure 1*). The CD8 dynamics are similar to those generated by CD8⁺ T cell model. However, the alternate model underestimates the data at day seven and the sharp decline between 7–8 d. While it is inappropriate to directly compare these models due to the varying number of data points, we assessed their goodness of fit with and without contributions from the data at 3–5 d pi (*Supplementary file 1*). Regardless of the data inclusion or exclusion, the alternate model had a higher AIC in all contexts and, thus, is not statistically justifiable. Similarly, we examined the model in *Baral et al., 2019* (*Equation (A7)-(A8)*), which also could not replicate our data (*Appendix 1—figure 1*).

$$\frac{dI}{dt} = \kappa_b I \left(1 - \frac{I}{I_{max}}\right) - \delta_{Eb} IE \tag{A7}$$

$$\frac{dE}{dt} = \eta_b \frac{IE}{K_{Eb} + I} - d_{Eb} \frac{IE}{K_{Db} + I} \tag{A8}$$
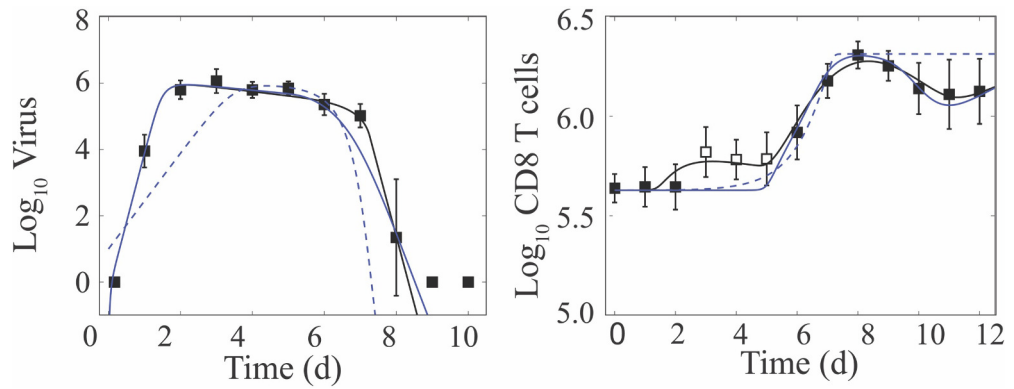
Appendix 1—figure 1. Fit of alternate CD8$^+$ T cell models. Fit of the CD8$^+$ T cell model (*Equation (1)-(6)*; solid black line) compared to the fit of two alternate CD8$^+$ T cell models (*Equation (A1)-(A6)* (solid blue line) and *Equation (A7)-(A8)* (dashed blue line)) to virus and CD8$^+$ T cells (excluding 3–5 d pi; white squares) from the lungs of mice infected with 75 TCID$_{50}$ PR8 (10 mice per time point). Resulting parameter values were $\delta_{Ea} = 4.02 \times 10^{-6}$ CD8$_E^{-1}$d^{-1}, $\eta_{Ea} = 3.12 \times 10^5$ CD8$_E$/d, and $K_{Ea} = 9.53 \times 10^5$ infected cells, and $\kappa_b = 3.33$ d^{-1}, $I_{max} = 1.0 \times 10^6$ infected cells, $\delta_{Eb} = 1.53 \times 10^{-5}$ CD8$_E^{-1}$d^{-1}, $\eta_b = 1.49$ d^{-1}, $K_{Eb} = 9.5$ infected cells, $d_{Eb} = 0.95$ d^{-1}, and $K_{Db} = 1.90 \times 10^6$ infected cells. All other parameters are in *Table 1*, and the AICs are in *Supplementary file 1*. Data are shown as mean $\pm$ standard deviation.

Appendix 2

Comparison of the Density-Dependent and CD8$^+$ T cell Models

We previously developed a density-dependent (DD) viral kinetic model, which describes the biphasic decline of viral loads without inclusion of specific host responses (**Smith et al., 2018**). This model tracks four populations: susceptible epithelial ('target') cells (T), two classes of infected cells (I_1 and I_2), and virus (V) (**Smith et al., 2018**).

$$\frac{dT}{dt} = -\beta TV \tag{A9}$$

$$\frac{dI_1}{dt} = \beta TV - kI_1 \tag{A10}$$

$$\frac{dI_2}{dt} = kI_1 - \delta_d(I_2)I_2 \tag{A11}$$

$$\frac{dV}{dt} = pI_2 - cV \tag{A12}$$

Briefly, in the DD model, virus-producing infected cells (I_2) are cleared according to the function $\delta_d(I_2) = \delta_d/(K_\delta + I_2)$, where δ_d/K_δ is the maximum per day rate of infected cell clearance and K_δ is the half-saturation constant (**Appendix 2—figure 1**). All other terms are common to the CD8 T$^+$ cell model (**Equation (1)-(6)**). The DD model provides a close fit to the viral load data in **Figure 1B** and replicates the biphasic viral load decline while excluding the dynamics of specific immune responses (**Smith et al., 2018**). Unsurprisingly, the CD8$^+$ T cell model is also capable of reproducing the biphasic viral load decay (**Figure 1B** and **Appendix 2—figure 1**). In that model, infected cell clearance is split into terms for non-specific clearance (δ) and CD8$_E$-mediated clearance ($\delta_E(I_2, E) = \delta_E E/(K_\delta + I_2)$) (**Appendix 2—figure 1**).

Because the CD8$^+$ T cell model is more mechanistic than the DD model, most of the correlations between the parameters common to both models (i.e., the rates of virus infectivity (β), virus production (p), and virus clearance (c)) were reduced (**Appendix 2—figure 1A**). In addition, the correlations between the infected cell clearance parameters (δ_d and K_δ or δ_E and K_{δ_E}) and between the rate of virus infectivity (β) and their ratios (δ_d/K_δ or δ_E/K_{δ_E}) were abolished (**Figure 2—figure supplement 1–2**). There was a negative correlation between the infected cell clearance parameters (δ and δ_E; **Figure 2B**), which may reflect the connection between the efficacy of early immune mechanisms and the CD8$^+$ T cell response. This result is in line with experimental evidence that the innate immune responses modulate the activation of adaptive immunity (**Iwasaki and Medzhitov, 2015**; **Luster, 2002**; **Iwasaki and Medzhitov, 2010**; **Le Bon and Tough, 2002**; **Jain and Pasare, 2017**).

The differences in model structure between the two models yielded changes in parameter sensitivity and model behavior during the rapid viral clearance phase (**Appendix 2—figure 1**). In the DD model, the most sensitive parameter is the infected cell clearance, δ_d (**Appendix 2—figure 1**). A 50% decrease in this parameter resulted in a ~7 d delay in viral resolution (**Appendix 2—figure 1**; **Smith et al., 2018**). In the CD8$^+$ T cell model, however, viral resolution is delayed by <1 d if the CD8$_E$-mediated infected cell clearance parameter (δ_E) is reduced by 50% (**Appendix 2—figure 1**, **Appendix 3—figure 1**). The rates of CD8$_E$ expansion (η) and decay (d_E) are sensitive and, thus, significantly influence the viral resolution kinetics (**Figures 1–2**). A 50% decrease in η results in a ~6 d delay in recovery (**Appendix 2—figure 1**, **Appendix 3—figure 1**) whereas a 48% decrease in η prolongs the infection by ~30 d (**Figure 3D–E**). This bifurcation in recovery time is a unique feature of the CD8$^+$ T cell model.
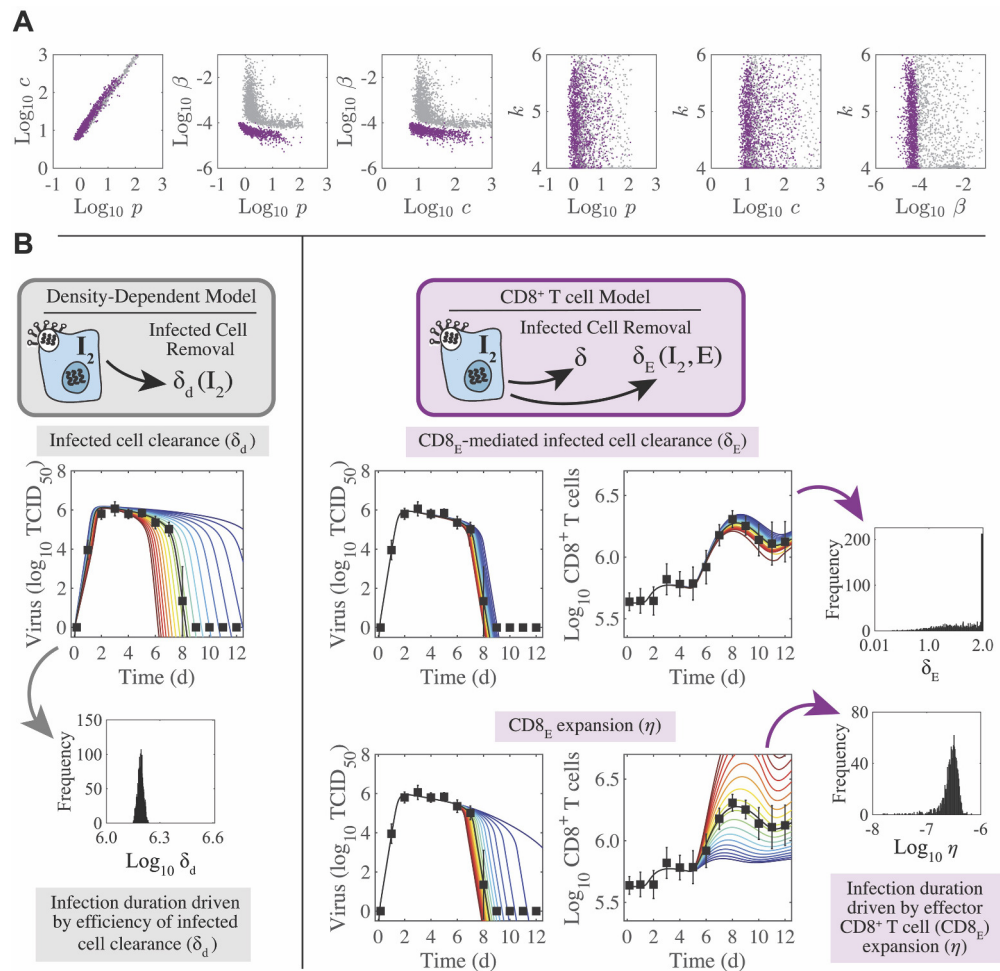
Appendix 2—figure 1. Parameter behavior of the density-dependent model and the CD8^{+} T cell model. (**A**) Comparison of parameters that were common between the density-dependent model (gray, *Equation (A9)-(A12)*) and the CD8^{+} T cell model (purple, *Equation (1)-(6)*). Correlations were evident between parameters relating to the rates of virus infectivity (β), virus production (p), and virus clearance (c). However, the strength of the correlation was significantly reduced in the CD8^{+} T cell model. The eclipse phase parameter (k) was not well-defined in either model. (**B**) In the density-dependent model (gray), the viral kinetics and the infection duration were sensitive to small changes in the infected cell clearance parameter (δ_d). This parameter was well-defined with a narrow 95% CI. In the CD8^{+} T cell model (purple), changing the $CD8_E$-mediated infected cell clearance parameter (δ_E) had little impact on viral kinetics or CD8^{+} T cell kinetics. However, these kinetics were most sensitive to changes in the rate of $CD8_E$ expansion (η), which was well-defined with a narrow 95% CI.
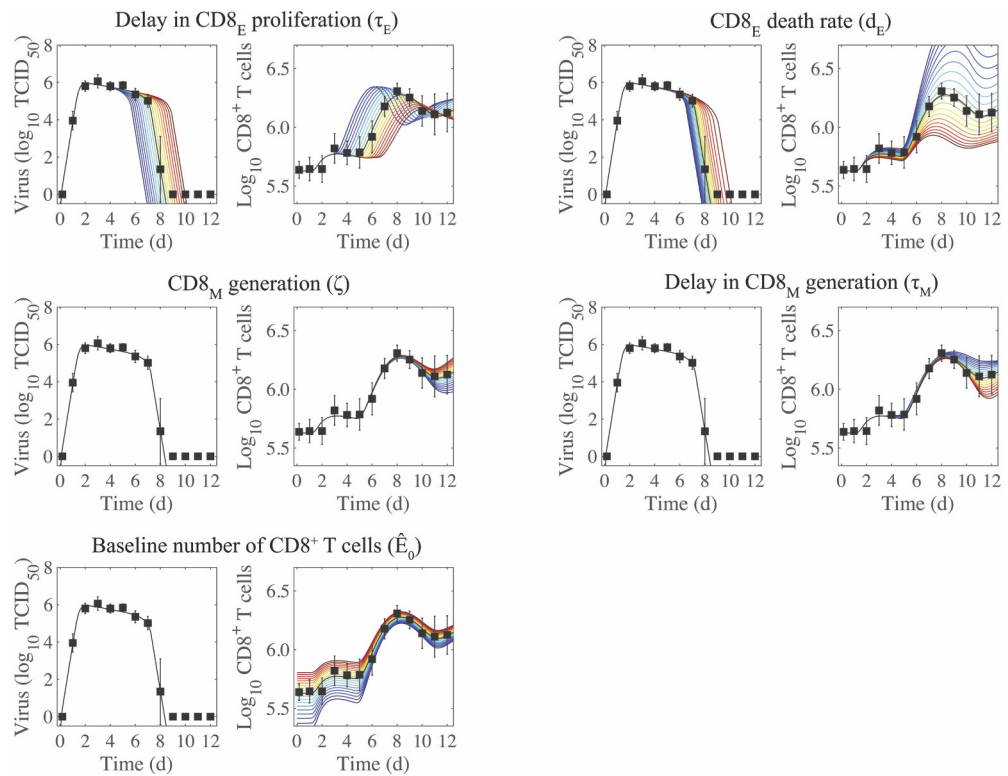
Appendix 3

Regulation of the CD8⁺ T cell Response

To further understand the regulation of the CD8$^+$ T cell response, we examined the 2-D parameter ensembles (*Figure 2A–C*, *Figure 2—figure supplements 1–2*) and the results from the sensitivity analysis (*Appendix 3—figure 1–2*). Overall, few parameters were correlated. There was an expected, although small, positive correlation between the rate of CD8$_E$ infiltration (ξ) and the associated half-saturation constant (K_E) (*Figure 2—figure supplement 1–2*), which represents the coordination between CD8$_E$ recruitment and the processes that prevent an overabundance of these cells. Likewise, a negative correlation was detected between the rate of initial CD8$_E$ influx (ξ) and the initial number of CD8$^+$ T cells ($\hat{E}_0$) (*Figure 2—figure supplements 1–2*). The influx rate (ξ) was also positively correlated with the delay in CD8$_E$ expansion (τ_E) (*Figure 2—figure supplements 1–2*). The rates of CD8$_E$ expansion (η) and decay (d_E) are correlated (*Figure 2C*), indicating a balance between these two processes. This correlation was expected and reflects the coordination of mechanisms that regulate CD8$^+$ T cell numbers, which may be necessary to limit excessive immunopathology while still resolving the infection (*Moskophidis and Kioussis, 1998*; *Duan and Thomas, 2016*; *La Gruta et al., 2007*). Further, because of this correlation and the sensitivity of η (*Appendix 3—figure 1*), the CD8$^+$ T cell kinetics are sensitive to changes in d_E (*Appendix 3—figure 1*). However, increasing the decay rate had less impact on the viral load kinetics, comparatively. Because d_E is correlated with both η and the rate of CD8$_M$ generation (ζ) (*Figure 2C*), it naturally follows that η and ζ are correlated (*Figure 2—figure supplements 1–2*). Changing the rates of virus infectivity (β), production (p), or clearance (c) had little effect on viral load or CD8$^+$ T cell kinetics (*Appendix 3—figure 1*).
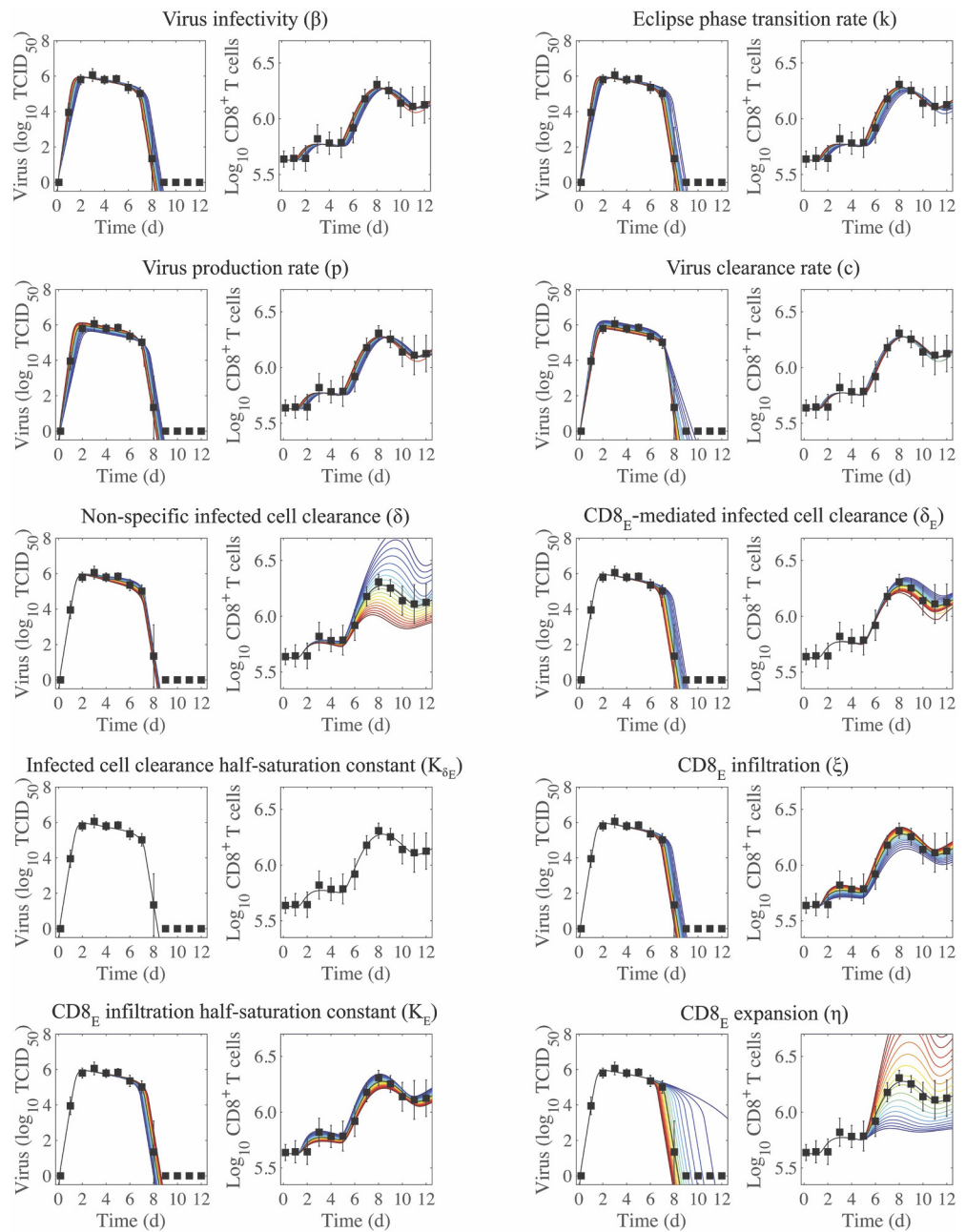
Appendix 3—figure 1. Sensitivity of the CD8$^+$ T cell model. Solutions of the CD8$^+$ T cell model (*Equation (1)-(6)*) with the indicated parameter (β, k, p, c, δ, δ_E, K_{δ_E}, ξ, K_E, or η) increased (red) or decreased (blue) 50% from the best-fit value (*Table 1*). CD8$_E$ denotes effector CD8$^+$ T cells.

Appendix 3—figure 2. Sensitivity of the CD8$^+$ T cell model. Solutions of the CD8$^+$ T cell model (*Equation (1)-(6)*) with the indicated parameter (τ_E, d_E, ζ, τ_M, or $\hat{E}_0$) increased (red) or decreased (blue) 50% from the best-fit value (*Table 1*). CD8$_E$ and CD8$_M$ denote effector and memory CD8$^+$ T cells, respectively.